Mind the gaps: Emergence of blenders in a three-dimensional Hénon-like map with different orientation properties

Dana C'Julio, Bernd Krauskopf and Hinke M. Osinga Department of Mathematics, The University of Auckland Private Bag 92019, Auckland 1142, New Zealand

Abstract

The generalisation of Smale's horseshoe construction in spaces of at least dimension three can lead to a type of hyperbolic set called a blender. The characterising feature of a blender is that it has an invariant manifold that behaves as a geometric object of a higher dimension than expected from the dimension of the manifold itself. The presence of a blender can be used to prove the robust existence of a nontransverse heterodimensional cycle, leading to robust nonhyperbolic chaotic dynamics, also known as wild chaos. We consider a Hénon-like family of maps, which is one of the only known explicit examples that exhibits a blender generated by a three-dimensional horseshoe. We investigate how the orientation properties of the map affect the creation of a blender. To this end, we use advanced numerical techniques to compute the stable or unstable manifolds of the fixed points and period-two orbits of the map; these manifolds are a key element in the creation of a blender. We discover that the organisation of the manifolds, and hence, the blender, follow a consistent pattern as the parameters are varied, and we show in detail the order of events that bring about the generation or disappearance of blenders. This allows us to obtain an estimate for the lower bound of the parameter value at which a blender arises in this map. In particular, we contrast the results of the different orientation properties of the map, which is essential for understanding how blenders lose or gain their defining properties as parameters change.

1 Introduction

Uniform hyperbolicity, first introduced by Anosov [5] and Smale [49], is one of the most studied forms of chaotic dynamics. A uniformly hyperbolic system has a nonwandering set with a tangent bundle that has a continuous decomposition into stable and unstable subspaces; hence, the nonwandering set has stable and unstable manifolds of well-defined, fixed dimensions. Uniform hyperbolicity is a structurally stable property under C^1 -perturbations and hence, C^1 -robust. Moreover, it was conjectured by Smale and others that any chaotic dynamical system could be turned into a uniformly hyperbolic system by a small perturbation, which would mean that uniform hyperbolicity is the 'typical case' of chaotic dynamics [10, 13]. While this is true for two-dimensional diffeomorphisms and three-dimensional flows [1], this early hope in the field turned out to be false in higher dimensions.

It was not until the late 1990s that nonuniform hyperbolic chaotic dynamics were shown to exist C^1 -robustly in systems of higher dimension [10, 11]. More specifically, in diffeomorphisms of dimension at least three and, equivalently, flows of dimension at least four, the existence of homoclinic tangencies and/or heterodimensional cycles — which are specific examples of nonuniformly hyperbolic dynamics — may be a persistent phenomenon under C^1 -perturbations. Hence, these objects are not exceptional but exist in C^1 -open regions of parameter space [45, 10]. This type of dynamics is also referred to as wild chaos [44]; see [7, 21, 23, 38, 32, 52] for examples. Since these more complicated forms of nonhyperbolic chaotic dynamics are robust, they could conceivably be observed in physical processes. Indeed, it has been observed that many of the chaotic phenomena seen in systems occurring in practice are nonhyperbolic [46].

The robustness of heterodimensional cycles is counterintuitive. Each individual heterodimensional cycle is of codimension at least one, which means that any generic C^1 -perturbation

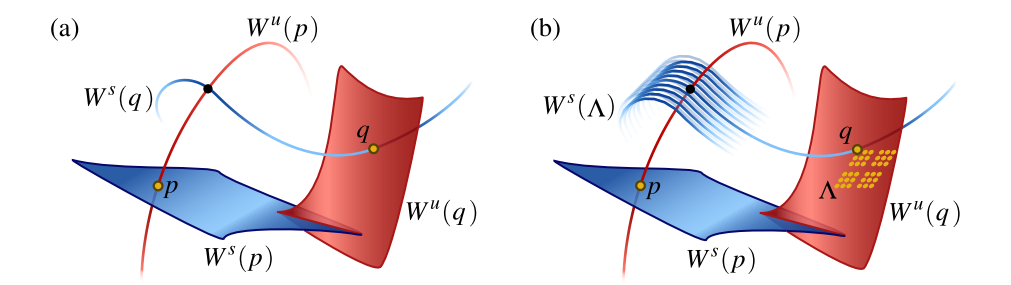


Figure 1: Sketch of a heterodimensional cycle of a three-dimensional map between two saddle fixed points p and q of different index, with (two-dimensional) stable manifolds $W^s(p)$ and (one-dimensional) unstable manifolds $W^u(p)$, and (one-dimensional) stable manifolds $W^s(q)$ and (two-dimensional) unstable manifolds $W^u(q)$. Panel (a) shows a nonrobust transverse heterodimensional cycle, and panel (b) is a robust transverse heterodimensional cycle, mediated by the stable manifold $W^s(\Lambda)$ of a blender Λ .

breaks it. Bonatti and Díaz showed that, nevertheless, there exists some (other) heterodimensional cycle for any diffeomorphism in a C^1 -neighbourhood of the initial diffeomorphism [9]. To prove this result, they introduced the concept of a blender. A blender is a transitive hyperbolic set Λ for which, say, the k-dimensional stable manifold $W^s(\Lambda)$ acts as an object of dimension larger than k.

In the lowest-dimensional case of a three-dimensional diffeomorphism, this means that the one-dimensional invariant manifold $W^s(\Lambda)$ cannot be avoided by one-dimensional curves from (a C^1 -open neighbourhood of) a particular direction [10], which is illustrated in [8] with an affine construction. This property and, hence, the blender itself is C^1 -robust, and this implies the existence of robust heterodimensional cycles when, say, the one-dimensional unstable manifold of a hyperbolic set of different unstable dimension intersects $W^s(\Lambda)$, leading to wild chaotic dynamics; see also [12, 10, 17]. Figure 1 shows an illustrative sketch of a heterodimensional cycle between two saddle fixed points p and q of different index (number of unstable directions). In panel (a), their two-dimensional stable and unstable manifolds $W^s(p)$ and $W^u(q)$ intersect transversally and, hence, this intersection is robust. However, their one-dimensional manifolds $W^{u}(p)$ and $W^{s}(q)$ intersect in a nontransverse way: any generic C^{1} -perturbation will break this connection, that is, the overall heterodimensional cycle. The situation for the fixed points pand q in Figure 1(b) is identical, but now the saddle q is part of a hyperbolic set Λ that is a blender. Its stable manifold $W^s(\Lambda)$ therefore 'behaves like a surface' in that it cannot be avoided by $W^{u}(p)$, as the sketch attempts to illustrate. Any generic C^{1} -perturbation will therefore still break the heterodimensional cycle between p and q, but there is then a heterodimensional cycle between p and a (typically) different point in Λ .

Blenders come in different flavours, are conceptually rich, and of great impact in the theory of robust nonhyperbolic chaos — yet they remain largely abstract constructions. The most 'hands-on' blender, called a blender-horseshoe [10, 16, 8], is a direct generalisation of Smale's horseshoe construction [49] to dimension at least three. In fact, the first and practically only example in the literature of a blender of an explicitly defined diffeomorphism is of this type. Namely, a blender-horseshoe was shown to exist in an extension of the Hénon map [33] to \mathbb{R}^3 that was introduced in [34]; see also [16, 35, 36]. This Hénon-like family of diffeomorphisms takes the form

$$\mathcal{H}(x,y,z) = (y, \alpha - y^2 - \beta x, \xi z + y), \tag{1}$$

and extends the planar Hénon map

$$h(x,y) = (y, \alpha - y^2 - \beta x) \tag{2}$$

acting on the (x, y)-plane with an affine shear in the third variable z. Note that (1) has skew-product structure because z does not appear in the equations for x and y.

The Hénon-like map (1) is our central object of study. Throughout, we focus on the case that h has an invariant hyperbolic set Λ_h in the form of a full Smale horseshoe with dynamics conjugate to a full shift on two symbols. This can be achieved by setting $\alpha = 4.2$ and $\beta = \pm 0.3$, which are the parameter values we use throughout. The sign of β is important here: for $\beta > 0$ the map h is orientation-preserving, and for $\beta < 0$ it is orientation-reversing; this has implications for the nature of the hyperbolic set Λ_h and, hence, the corresponding hyperbolic set Λ of the three-dimensional map \mathcal{H} ; see Section 2. Moreover, we consider the case of expansion in the z-direction, as given by the eigenvalue $|\xi| > 1$; note that the sign of ξ also affects the orientation properties of Λ . In this setting, the one-dimensional stable manifold $W^s(\Lambda)$ of the associated hyperbolic set Λ of \mathcal{H} has dimension one, and we are interested in its geometric properties. Further relevant properties of this family of three-dimensional diffeomorphisms are reviewed in Section 2.3.

According to the theory [16], the hyperbolic set Λ of \mathcal{H} is expected to be a blender when $|\xi|$ is sufficiently close to 1. In fact, it was proved in [34] that this Hénon-like map has a blender for $\alpha = 9.5$, $\beta = -0.1$ and $\xi = 1.185$. A subsequent computer-assisted proof in [14] validated required covering relations and cone conditions to establish the existence of a blender for $\alpha = 9.5$, $\beta = -0.3$ and $\xi \in [1.01, 1.125]$. Moreover, numerical evidence has been presented in [34, 35] to show that a blender still exists for considerably larger values of ξ , and this was achieved in the following way. In the context of this three-dimensional setting, a blender is characterised by the property that the one-dimensional stable manifold $W^s(\Lambda)$ behaves like a surface when viewed from an open set of directions. More precisely, the closure of the projection of $W^s(\Lambda)$ along a fixed, appropriate direction has nonempty interior; moreover, this property persists in a C^1 -open neighbourhood of such a projection. It is not possible to compute $W^s(\Lambda)$ in its entirety to check this property because $W^s(\Lambda)$ comprises the one-dimensional stable manifolds of all the uncountably many points in Λ . However, since periodic points are dense in Λ , one may equivalently check that the one-dimensional stable manifold $W^{s}(p)$ of any fixed or periodic point p has a dense projection. This characterising property of a blender is referred to as the *carpet* property [34, 35] because the curve $W^s(p)$ weaves back and forth in phase space to generate (the impression of) a surface.

The carpet property can be tested effectively by computing a sufficiently long piece of a selected (one-dimensional) stable manifold as an arclength parametrised curve and determining its intersection set with a suitable cross-section. The existence of a blender can then be established by checking that the largest gaps in a suitable projection of the intersection set converge to zero as the arclength of the computed manifolds increases. This approach was used to show that the Hénon-like map \mathcal{H} has a blender up to $\xi = 1.843$ for $\beta = -0.1$ [34] and up to $\xi = 1.75$ for $\beta = -0.3$ [35], both with $\alpha = 9.5$. For large expansion rates $|\xi| \gg 1$, however, Λ will not be a blender, but rather have a Cantor-like structure when seen from any direction. In this case, the gaps in the projection do not close with increasing arclength of the one-dimensional manifold.

Motivated by this dichotomy, we address the following two practical and natural questions:

How exactly is the blender lost when ξ is increased, or created when ξ is decreased?

Do the orientation properties of the map have an impact on the creation or loss of a blender?

Note that the methods of proof in [34] as well as the computer-assisted approach in [14] run into difficulties with verifying required properties near where the blender is lost. Likewise, the approach in [34, 35] of considering the convergence to zero or not of (a number of) the largest gaps becomes inaccurate near where the carpet property is lost. In particular, it is not clear from this previous work how exactly gaps open or close in the transition between blender

and nonblender as ξ is increased or decreased, respectively. Furthermore, the influence of the orientation properties of the map \mathcal{H} on this process remains unexplored in the literature.

This realisation motivates the work presented here. To address these issues and answer the above questions, we employ a refined method for the computation of a one-dimensional (stable) manifold that ensures that its intersection points with a chosen section are ordered reliably along the manifold. This then allows us to identify how individual points of the intersection set depend on the contraction rate ξ of the map \mathcal{H} . Our computational approach is presented and validated in [15]; it builds on the approach in [34, 35], also uses compactification of the phase space to a cylinder, and includes a number of key improvements in terms of its data structure, accuracy and efficiency. As we will show in Sections 3 and 4, it allows us to find and present individual intersection points of interest as ξ -parametrised curves.

The study of these intersection curves is the key to understanding how gaps close and a blender is created as $|\xi|$ is decreased towards 1. When the set of intersection curves appears to fill a solid region in the (ξ, z) -plane, then the associated manifold has the carpet property over an interval of ξ -values and, hence, the hyperbolic set Λ is a blender. In particular, our computational approach enables us to determine which intersection points bound which gaps in projection. The intersection points that bound the gaps for large $|\xi|$ are those that also bound the gaps of the standard two-dimensional Hénon map. However, this turns out not to be the case for smaller values of ξ near where the gaps close. We show that this is due to a 'switching of boundaries of gaps,' which occurs over an intermediate ξ -range. Before the gaps actually close, this switching 'stabilises' and we are able to identify exactly which intersection points bound which gaps. This allows us to identify their moment of closing by considering only the respective two curves of boundary points. In this way, we show that gaps close one-by-one in a sequence with an asymptotic contraction rate and a well-defined limit that provides the best estimate for the ξ -value up to which the carpet property holds (with respect to the chosen projection direction).

This general scenario occurs for all four cases of orientation of \mathcal{H} as given by the signs of β and ξ . However, there are differences regarding which intersection points bound the (biggest) gaps of interest, and we represent this topological information for each case in the form of a recurrence relation. In particular, we find that the gaps of interest are bounded, near where they close, by the stable manifolds of the two fixed points of \mathcal{H} when ξ is positive, while they are bounded by the stable manifold of its period-two point when ξ is negative.

The paper is structured as follows. In Section 2 we provide further information on the Hénon-like family (1). We show where full horseshoe dynamics can be found in the planar Hénon map and what the structure of the invariant manifolds is for both the orientation-preserving case with $\beta > 0$ and the orientation-reversing case with $\beta < 0$; we then provide more information on the map \mathcal{H} and explains the compactification of its phase space to a cylinder. Section 3 considers the case of an orientation-preserving shear, that is, $\xi > 0$. To set the stage, we first show illustrations of a blender and a non-blender for both $\beta > 0$ and $\beta < 0$. The transition to a blender for the orientation-preserving case with $\beta > 0$ is then discussed in Section 3.1, and that for the orientation-reversing case with $\beta < 0$ in Section 3.2. In Section 4, we then consider in the same way the transition to a blender for an orientation-preserving shear, where Section 4.1 presents the case with $\beta > 0$ and Section 4.2 that with $\beta < 0$. Finally, in Section 5, we draw some conclusions and point to directions for future work.

2 Properties of the Hénon-like family

We now provide further information on the planar Hénon map h, its associated full horseshoe, and its extension to the three-dimensional diffeomorphism \mathcal{H} . For general background information on dynamical systems, we refer to the relevant literature, for example, [41, 50, 31, 4, 47].

| Orientation-preservin | g h with | $\alpha = 4.2$ a | and $\beta =$ | 0.3 |
|--------------------------------------------------|-----------|--------------------|---------------|-----|
| $p_h^- = (-2.8, -2.8),$ $p_h^+ = (1.5, 1.5),$ | | 0.0541, $-0.1036,$ | | |
| O: 44: | 1 | , | 2 | |

Orientation-reversing h with $\alpha = 4.2$ and $\beta = -0.3$ $p_h^- = (-2.4291, -2.4291), \quad \lambda_1^- = -0.0610 \quad \lambda_2^- = 4.9191, \\ p_h^+ = (1.7291, 1.7291), \quad \lambda_1^+ = 0.8468, \quad \lambda_2^+ = -3.5428.$

Table 1: Location and eigenvalues of the fixed points p_h^- and p_h^+ of h for $\alpha=4.2$, with $\beta=0.3$ in the first block, and $\beta=-0.3$ in the second block.

2.1 The standard Hénon map

There are many equivalent ways to express the Hénon map. The advantage of the Hénon-like family \mathcal{H} as presented in (1) is that its restriction h to the (x,y)-plane has the form of the standard Hénon map as defined in [28] (see also [22]). This standard form can be obtained from the Hénon map as given in [33] via the parameter and coordinate transformation

$$(u,v) \mapsto (\frac{1}{\alpha}y, -\frac{\beta}{\alpha}x), \quad (a,b) \mapsto (\alpha, -\beta).$$

The map h has the two fixed points

$$p_h^{\pm} = \left(\rho^{\pm}, \rho^{\pm}\right),\tag{3}$$

where

$$\rho^{\pm} = \frac{1}{2} \left(-1 - \beta \pm \sqrt{4\alpha + (1+\beta)^2} \right). \tag{4}$$

These fixed points exist provided $4\alpha + (1+\beta)^2 \ge 0$, and their eigenvalues are

$$\lambda_1^{\pm} = -\rho^{\pm} + \sqrt{(\rho^{\pm})^2 - \beta} \quad \text{and} \quad \lambda_2^{\pm} = -\rho^{\pm} - \sqrt{(\rho^{\pm})^2 - \beta}.$$
 (5)

Additionally, the map h has a unique period-two orbit, denoted $p_{h,2} = \{p_{h,2}^1, p_{h,2}^2\}$, with

$$p_{h,2}^1 = (\rho_2^-, \rho_2^+) \quad \text{and} \quad p_{h,2}^2 = (\rho_2^+, \rho_2^-),$$
 (6)

where

$$\rho_2^{\pm} = \frac{1}{2} \left(1 + \beta \pm \sqrt{4\alpha - 3(1+\beta)^2} \right). \tag{7}$$

It exists provided $4\alpha - 3(1+\beta)^2 \ge 0$ and has the two eigenvalues

$$\lambda_1^2 = A - \sqrt{A^2 - \beta^2}$$
 and $\lambda_2^2 = A + \sqrt{A^2 - \beta^2}$, (8)

where $A = 2(1 - \alpha) + \beta(3 + 2\beta)$.

The determinant of the Jacobian matrix of h is β . Hence, for the choice of parameters $\alpha=4.2$ and $\beta=\pm0.3$ that we consider throughout, the map h is orientation-preserving for $\beta>0$ and orientation-reversing for $\beta<0$. The coordinates of p_h^\pm and their eigenvalues are shown in Table 1 for $\alpha=4.2$, $\beta=0.3$ and for $\alpha=4.2$, $\beta=-0.3$. Note that both p_h^- and p_h^+ are saddles for these parameter choices, with one-dimensional stable and unstable manifolds $W^s(p_h^\pm)$ and $W^u(p_h^\pm)$, respectively. Moreover, we have the following two cases, depending on the orientation properties of the map h:

- 1. $\beta > 0$ (orientation-preserving case): both eigenvalues of p_h^- are positive, meaning that $W^s(p_h^-)$ and $W^u(p_h^-)$ are oriented. Both eigenvalues of p_h^+ are negative, and hence, $W^s(p_h^+)$ and $W^u(p_h^+)$ are nonoriented.
- 2. $\beta < 0$ (orientation-reversing case): both fixed points p_h^- and p_h^+ have one positive and one negative eigenvalue. Specifically, $W^u(p_h^-)$ and $W^s(p_h^+)$ are oriented, and $W^s(p_h^-)$ and $W^u(p_h^+)$ are nonoriented.

2.2 Full horseshoe in the standard Hénon map

To find a blender-horseshoe of \mathcal{H} , the first step is to determine when the planar diffeomorphism h has a transitive hyperbolic set Λ_h with dynamics that are topologically equivalent to a full horseshoe. Figure 2 illustrates where in the (α, β) -plane this is the case and what the horseshoe looks like for the orientation-preserving and the orientation-reversing cases.

Panel (a) of Figure 2 shows part of the bifurcation diagram of h shown in [28, 43], with only the bifurcation curves that are relevant for identifying the regions with a full horseshoe. In addition to the bifurcation curves obtained in [28, 43], we also show the curves Hom_{Λ} and Het_{Λ} that delimit the region $\Omega_o \cup \Omega_n$, where h has a full horseshoe. These additional curves were computed with a boundary value problem setup in MATCONTM [42]. Panels (b1) and (c1) of Figure 2 provide a schematic representation of the full horseshoe in Ω_o and Ω_n , and panels (b2) and (c2) show the relevant computed manifolds $W^s(p^{\pm})$ and $W^u(p^{\pm})$ of p^{\pm} for $(\alpha, \beta) = (4.2, 0.3) \in \Omega_o$ and $(\alpha, \beta) = (4.2, -0.3) \in \Omega_n$, respectively.

For the existence of a full horseshoe, both p_h^- and p_h^+ must exist and be saddles. The points p_h^\pm of h exist for α -values to the right of the curve SN of saddle-node bifurcation in Figure 2(a). Initially, for $\beta > -1$, the fixed point p_h^- is a saddle, and p_h^+ is a sink, whereas, for $\beta < -1$, the fixed point p_h^- is a source and p_h^+ is a saddle. Only to the right of the curve PD, where p_h^+ (for $\beta > -1$) or p_h^- (for $\beta < -1$) undergoes a period-doubling bifurcation, both fixed points are saddles.

Note in Figure 2(a) that the codimension-two point SH is a 1:1 resonance point that gives rise to a Neimark-Sacker bifurcation (not shown); see [28] for further details. From SH emerges a wedge-like region of homoclinic tangles (shaded in purple), bounded by two curves of homoclinic bifurcation, labelled Hom, which represent the 'first' and 'last' homoclinic tangencies between $W^s(p_h^-)$ and $W^u(p_h^-)$. Similarly, there is a wedge-like region of heteroclinic tangles (shaded in blue), bounded by the curves Het that represent the 'first' and 'last' heteroclinic tangencies between $W^s(p_h^-)$ and $W^u(p_h^+)$; these curves originate from the codimension-two point SP, where the saddle-node bifurcation and the period-doubling bifurcation meet in a saddle-node-period-doubling point; see also [28]. Within the intersection set of the two wedge-like regions, both homoclinic and heteroclinic tangles coexist, implying the presence of infinitely many additional homoclinic and heteroclinic tangencies brought about by the intricate structure of $W^s(p_h^{\pm})$ and $W^u(p_h^{\pm})$.

A full horseshoe of h exists in the regions denoted Ω_o and Ω_n in Figure2(a), which are bounded the curves Hom_{Λ} of first homoclinic and Het_{Λ} of first heteroclinic tangency, respectively, between the corresponding invariant manifolds of p^{\pm} . In Ω_o and Ω_n , all stable and unstable manifolds of saddle objects intersect transversely to give rise to the hyperbolic set $\Lambda_h = \overline{W^s(p_h^{\pm})} \cap W^u(p_h^{\pm})$, where the overbar represents taking the closure. The topological nature of the horseshoe depends on the sign of β . In Ω_o , the map h is orientation-preserving and we speak of a nonoriented full horseshoe, and in Ω_n , it is orientation-reversing and we speak of a nonoriented full horseshoe. Panels (b1) and (c1) of Figure 2 are sketches of the oriented and nonoriented full horseshoe: the green square with vertices A-D (labelled anti-clockwise) is mapped by h to a horseshoe-like shape, whose vertices are accordingly labelled A-D. Additionally, the two saddle fixed points p_h^- and p_h^+ of the map h are marked as golden dots; also

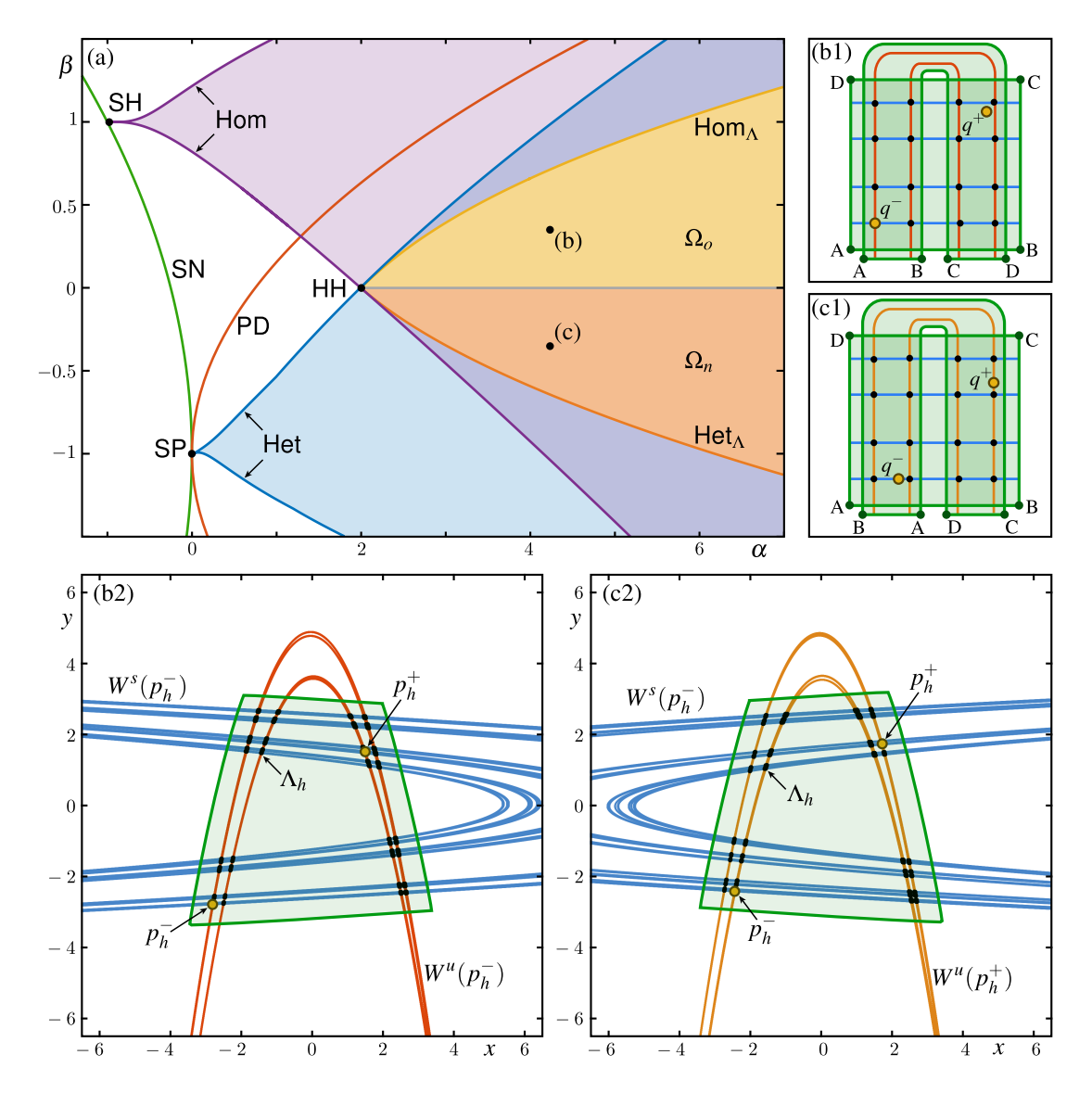


Figure 2: Partial bifurcation diagram and phase portraits in the regions Ω_o and Ω_n where the standard Hénon map (2) has an oriented and nonoriented full horseshoe, respectively. Panel (a) shows the (α, β) -plane for $\alpha \in [-1.5, 1.5]$ and $\beta \in [-1.25, 1.25]$ with the bifurcation curves SN, PD, Hom, Het, Hom, and Het, codimension-two points SH, SP and HH are marked by black dots. Panels (b1) and (c1) are sketches of the full horseshoe in Ω_o and Ω_n , respectively; shown are the fixed points p_h^- and p_h^+ (golden dots), their manifolds $W^s(p_h^-)$ (blue), $W^u(p_h^-)$ (red), $W^u(p_h^+)$ (orange), a part of the hyperbolic set Λ_h (black dots), and a green square with vertices A, B, C and D, and its image under h which contains Λ_h . Panels (b2) and (c2) show the computed manifolds $W^s(p_h^-)$ and $W^u(p_h^+)$ that generate the full horseshoe for $(\alpha, \beta) = (4.2, 0.3) \in \Omega_o$ and $(\alpha, \beta) = (4.2, -0.3) \in \Omega_n$, respectively.

shown are segments of the manifolds that form the accessible boundary [3, 18, 29, 30] of the full horseshoe, namely, segments of $W^s(p_h^-)$ (blue curve), $W^u(p_h^-)$ (red curve) and $W^u(p_h^+)$ (orange curve). The accessible boundary of the full horseshoe is formed by the invariant manifolds that generate the 'endpoints' of the Cantor set; they are also known as the invariant border of Λ_h (black dots) [25].

Note that both the green square and its image are labelled anti-clockwise for the oriented full horseshoe in Figure 2(b1). This configuration is the standard case of the Smale horseshoe

construction, which is commonly presented in textbooks such as [31, 41]. The fixed point p_h^- is situated at the corner of the full horseshoe, and the oriented manifolds $W^s(p_h^-)$ and $W^u(p_h^-)$ form its accessible boundary. In contrast, the point p_h^+ is positioned 'inside' Λ_h , and its manifolds $W^s(p_h^+)$ and $W^u(p_h^+)$ are not accessible; they are not shown in panel (b1). Note that the point p_h^- is also referred to as an (s, u)-boundary point [25]; where s and u allude to the fact that both its stable and unstable manifolds are accessible.

In contrast, for the orientation-reversing case shown in Figure 2(c1), the image of the green square has vertices A-D that are labelled clockwise. The square undergoes a reflection before being stretched into a horseshoe shape by h. While this is not the standard example typically shown in the literature, the main structure of this 'nonstandard' horseshoe can be found in [25], along with other Smale horseshoes of "new types"; see also [22]. Note in panel (c1) that the fixed points are in different positions compared to panel (b1); both now lie on a boundary of the full horseshoe. The manifolds that are the accessible boundary of the full horseshoe are now the nonoriented manifolds $W^s(p_h^-)$ and $W^u(p_h^+)$. For this type of horseshoe, the fixed point p_h^- is also referred to as an s-boundary point, and p_h^+ as a u-boundary point [25].

Panels (b2) and (c2) of Figure 2 show computed examples of the phase portraits for the orientation-preserving and orientation-reversing cases, respectively. Specifically, we show the relevant manifolds $W^s(p_h^-)$ and $W^u(p_h^\pm)$ at the parameter points marked as dots in panel (a). In Figure 2(b2) and (c2), the green quadrilateral represents the green square from the sketches with vertices A-D, which contains the hyperbolic set Λ_h (black dots) with the p_h^\pm (golden dots); see also [36]. Also shown are the invariant manifolds that form the respective accessible boundary: $W^s(p_h^-)$ (blue curve) and $W^u(p_h^-)$ (red curve) in panel (b2), and $W^s(p_h^-)$ (blue curve) and $W^u(p_h^+)$ (orange curve) in panel (c2). These one-dimensional global manifolds have been computed as arclength-parametrised curves up to considerable lengths; they repeatedly leave the green region of the (x,y)-plane, yet return and intersect each other transversally in countably many points, the closure of which is the hyperbolic set Λ_h .

We now compactify the two-dimensional phase space of h to the (inside) of the closed unit disk, denoted \mathcal{D} , via the transformation

$$T_h : \mathbb{R}^2 \to \mathcal{D}$$

$$(x,y) \mapsto (\bar{x},\bar{y}) := \left(\frac{x}{1+\sqrt{1+x^2+y^2}}, \frac{y}{1+\sqrt{1+x^2+y^2}}\right). \tag{9}$$

The phase portrait inside \mathcal{D} , which is known as the Poincaré disk, can be extended to its boundary, and points on $\partial \mathcal{D}$ correspond to directions of escape to infinity in the (x, y)-plane.

Considering the structure of the invariant manifolds on the Poincaré disk \mathcal{D} not only provides a global view of the dynamics, but also has a major computational advantage. The manifolds of the fixed points p_h^{\pm} (or any periodic point) make longer and longer excursions towards infinity in the (x, y)-plane as they pass through the central region near Λ_h . After compactification, however, all such excursions have bounded arclength, and this allows us to compute very long pieces of invariant manifolds reliably as curves that weave back and forth many times. This ability is a crucial ingredient for checking the carpet property of \mathcal{H} , and we extend the transformation T_h to \mathbb{R}^3 in Section 2.3; see also [15, 34, 35].

The respective horseshoe structure of h from Figure 2 is illustrated in Figure 3 in compactified (\bar{x}, \bar{y}) -coordinates on the Poincaré disk \mathcal{D} . Shown are the fixed points p_h^{\pm} and their manifolds $W^s(p_h^{\pm})$ and $W^u(p_h^{\pm})$, where panels (a1) and (b1) are sketches that 'extend' those in panels (b1) and (c1) of Figure 2, and panels (a2) and (b2) of Figure 3 show the computed objects on \mathcal{D} . On the outer circle $\partial \mathcal{D}$ there are two fixed points: the source s_h , which lies at (-1,0) for $\beta > 0$ and at (1,0) for $\beta < 0$, and the sink $q_h = (0,-1)$; these two points correspond to the asymptotic limits of certain branches of stable and unstable manifolds, respectively.

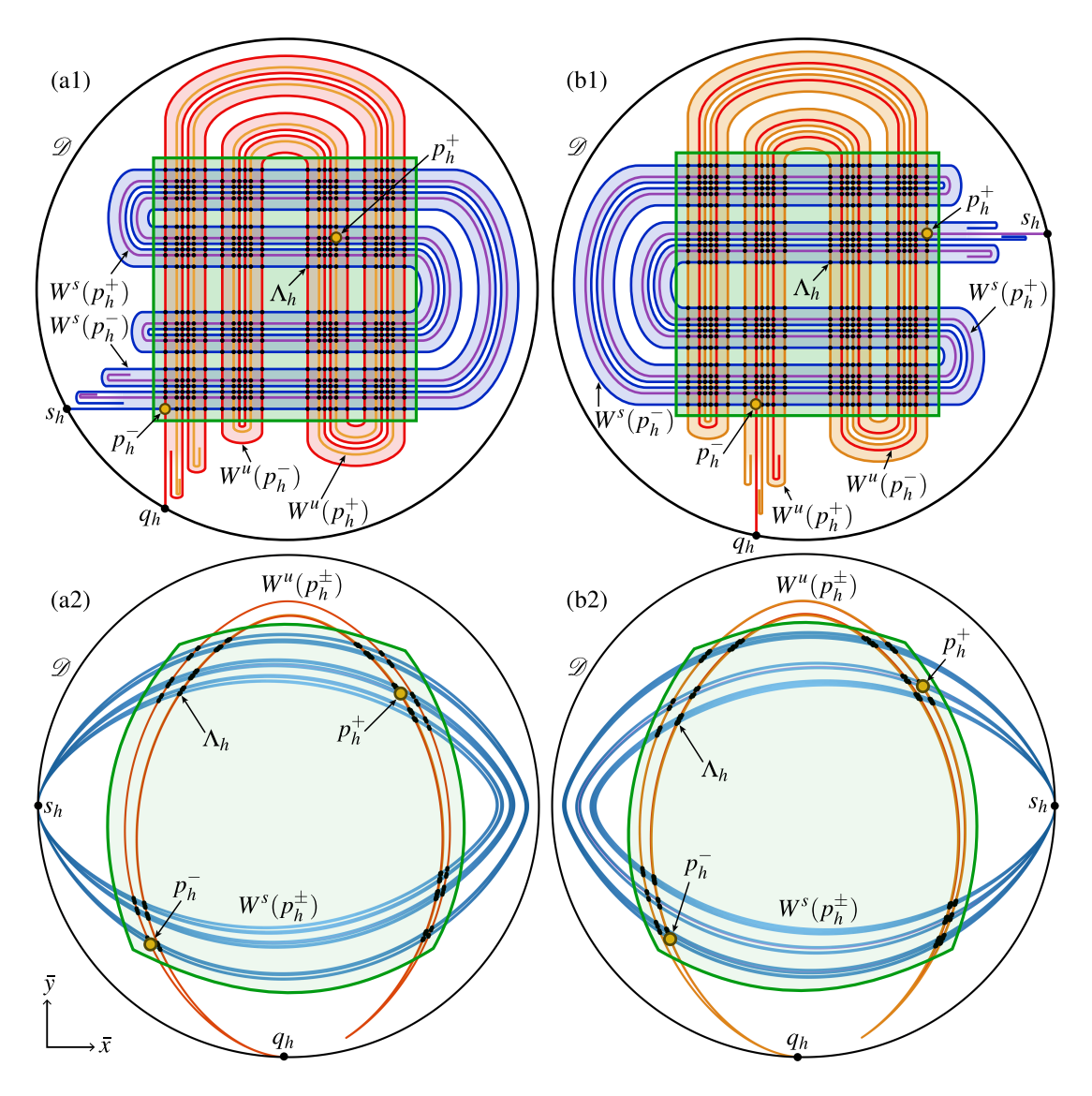


Figure 3: Phase portrait of h in the Poincaré disk \mathcal{D} , for $\beta > 0$ in the first column, and $\beta < 0$ in the second column. Panels (a1) and (b1) are a detailed sketch of the full horseshoe, and panels (a2) and (b2) are their numerical counterparts, for $\alpha = 4.2$, $\beta = 0.3$ and $\alpha = 4.2$, $\beta = -0.3$, respectively. Shown are the fixed points p_h^- and p_h^+ as golden dots, the manifolds $W^s(p_h^-)$ (blue), $W^u(p_h^-)$ (red) and $W^s(p_h^+)$ (purple) and $W^u(p_h^+)$ (orange). Also shown with black dots is part of the hyperbolic set Λ_h contained in the green region, the sink q_h and source s_h . The black circle represents the boundary of \mathcal{D} .

In the sketch for the case of an oriented full horseshoe in Figure 3(a1), the manifolds $W^s(p_h^{\pm})$ and $W^u(p_h^{\pm})$ are both oriented. One branch of $W^s(p_h^{-})$ goes directly to the source $s_h \in \partial \mathcal{D}$ and never returns to the green square and, similarly, one branch of $W^u(p_h^{-})$ goes directly to the sink $q_h \in \partial \mathcal{D}$; for ease of representation, s_h is shown here directly to the left of p_h^{-} and q_h directly below p_h^{-} . The other branches of $W^s(p_h^{-})$ and $W^u(p_h^{-})$ make excursions closer and closer to s_h and q_h , respectively, while weaving repeatedly through the central region, creating infinite sequences of accumulating manifold segments in the square. In contrast, the invariant manifolds of p_h^{+} are nonoriented: both branches of $W^s(p_h^{+})$ and $W^u(p_h^{+})$ map to one another under h and make excursions to near s_h and q_h , respectively, while weaving through the green square. Note that $W^s(p_h^{-})$ and $W^u(p_h^{-})$ are indeed accessible: from any point in the complement of $W^s(\Lambda_h)$

in \mathcal{D} , there exists a continuous path to p_h^- , or any point in $W^s(p_h^-)$ that does not cross $W^s(\Lambda_h)$, and likewise for $W^u(p_h^-)$. Figure 3(a2) shows these invariant objects as computed on \mathcal{D} for $\alpha=4.2$ and $\beta=0.3$; while the fine details of the Cantor structure cannot be distinguished at this scale, we checked and can confirm that overall structure and relative positions of the computed manifolds are as sketched in panel (a1). In particular, $W^s(p_h^{\pm})$ only accumulates on the point s_h where $\bar{y} < 0$, and not where $\bar{y} > 0$ as may be perceived at this scale.

Panels (b1) and (b2) of Figure 3 show the orientation-reversing case. As the sketch in panel (b1) shows, $W^u(p_h^-)$ is still oriented, one of its branches goes directly to the sink q_h , and its other branch of $W^u(p_h^-)$ makes repeated excursions to q_h while weaving through the central region. However, $W^u(p_h^-)$ is now no longer accessible because it is accumulated on both sides by the nonoriented manifold $W^u(p_h^+)$. In the same way, the now oriented manifold $W^s(p_h^+)$, with a branch that goes directly to s_h , is not accessible because it is accumulated on both sides by the now nonoriented manifold $W^s(p_h^-)$. Indeed, the nonoriented manifolds $W^s(p_h^-)$ and $W^u(p_h^+)$ form the accessible boundary. What the actual invariant objects look like when computed on the Poincaré disk \mathcal{D} is shown in Figure 3(b2) for $\alpha = 4.2$ and $\beta = -0.3$. Note that $W^s(p_h^+)$ now 'opens to the right' and the point s_h lies at (1,0); moreover, the most prominently visible manifold is $W^u(p_h^+)$, which is now accessible and accumulates on $W^u(p_h^-)$.

2.3 Three-dimensional Hénon-like map

The three-dimensional Hénon-like family \mathcal{H} of diffeomorphisms extends the Hénon map h by incorporating an affine shear in the additional variable z. The family \mathcal{H} as given by (1) reduces to the standard form of the Hénon map discussed in Section 2.1; it is the map defined in [34], subject to the coordinate transformation $(x, y, z) \mapsto (-x, -y, -z)$ and the change of parameters $(\alpha, \beta) \mapsto (-\mu, -\beta)$. Given that z does not appear in the equations for x and y in (1), this family exhibits a skew-product structure. Consequently, vertical lines are mapped to vertical lines, according to the Smale horseshoe dynamics in the (x, y)-plane.

The dynamics along the z-direction are characterised by contraction or expansion, determined by whether $|\xi| < 1$ or $|\xi| > 1$, respectively. The two fixed points p_h^{\pm} of h are lifted to the fixed points

$$p^{\pm} = \left(\rho^{\pm}, \rho^{\pm}, \frac{\rho^{\pm}}{1 - \xi}\right) \tag{10}$$

of \mathcal{H} with ρ^{\pm} given by (4). These fixed points have as eigenvalues the two eigenvalues λ_1^{\pm} and λ_1^{\pm} from (5) and the third eigenvalue $\lambda_3^{\pm} = \xi$. Similarly, the period-two orbit of h from (6) lifts to the unique period-two orbit

$$p_2^{1,2} = \left(\rho_2^{\mp}, \rho_2^{\pm}, \frac{\rho_2^{\mp} + \xi \rho_2^{\pm}}{1 - \xi^2}\right),\tag{11}$$

of \mathcal{H} with ρ_2^{\pm} given by (7), whose eigenvalues are those in (8) and ξ^2 . In the same way, the entire hyperbolic set Λ_h lifts to the hyperbolic set Λ of \mathcal{H} , which can be obtained as the closure of $W^s(p^{\pm}) \cap W^u(p^{\pm})$.

As we will see, orientation and accessibility properties play an important role in determining how blenders of \mathcal{H} are created or lost. The determinant of the Jacobian matrix of \mathcal{H} is $\beta \xi$. Thus, the orientation of the map \mathcal{H} is not solely determined by β but also influenced by the sign of ξ . Hence, there are four cases determined by the signs of β and ξ . Previous research, including that in [34, 35, 36], considered the orientation-reversing case of \mathcal{H} where the underlying Hénon map is orientation revering and the shear is not, which corresponds to $\beta < 0$ and $\xi > 1$ in (1). This leaves open the question of how different orientation properties of the map \mathcal{H} affect the conditions under which Λ is a blender. Here, we explore all four distinct cases: first, the two cases of an orientation-preserving shear with positive ξ for either sign of β , and then those with

an orientation-reversing shear with negative ξ for either sign of β . Throughout, we consider an expansion rate $|\xi| > 1$, so that the stable manifolds of any periodic orbit and, indeed, $W^s(\Lambda)$ itself, are one dimensional and potentially have the carpet property.

As for the planar Hénon map, we compactify the three-dimensional phase space of \mathcal{H} , namely to the interior of the cylinder

$$C = D \times [-1, 1] = \{(x, y, z) \in \mathbb{R}^3 \mid ||(x, y)|| \le 1 \text{ and } ||z|| \le 1\},$$

which is achieved by the extension of the transformation T_h from (9) given by

$$T_{\mathcal{H}}: \mathbb{R}^3 \to \mathcal{C}$$

$$(x,y,z) \mapsto (\bar{x},\bar{y},\bar{z}) := \left(T_h(x,y), \frac{z}{1+\sqrt{1+z^2}}\right). \tag{12}$$

Throughout, we consider the compactified phase space \mathcal{C} and, for simplicity, we refer to the conjugate map $T_{\mathcal{H}} \circ \mathcal{H} \circ T_{\mathcal{H}}^{-1}$ as \mathcal{H} as well. On the boundary $\partial \mathcal{C}$ of the cylinder \mathcal{C} we find the following fixed points: the point $s^+ = (-1,0,1)$ for $\beta > 0$ or $s^- = (-1,0,-1)$ for $\beta < 0$, which each act as a saddle, and the points $q^{\pm} = (0,-1,\pm 1)$ (for any sign of β), which both act as sinks. Note that these points are the 'lifts' of the source s_h and the sink $q_h = (0,-1)$ on boundary $\partial \mathcal{D}$ of the Poincaré disk. We remark here that the existence of s^+ was erroneously reported in [34, 35] for $\beta < 0$.

3 Transition to a blender for an orientation-preserving shear

We first consider the case of $\xi > 0$ when the shear of the map \mathcal{H} is orientation-preserving; more specifically, we consider $\xi > 1$ so that the hyperbolic set Λ is of index 2 and, hence, its stable manifold has dimension one. We fix $\alpha = 4.2$ and examine two cases: in Section 3.1 we set $\beta = 0.3$ so that the planar full horseshoe and the map \mathcal{H} are orientation-preserving, and in Section 3.2 we set $\beta = -0.3$ so that the planar full horseshoe and \mathcal{H} are orientation-reversing. For each of these two cases, we investigate the structure of the relevant global stable manifolds to determine for which value of ξ a blender exists, and how it is created or lost when $\xi > 1$ is changed.

To set the stage, Figure 4 shows four phase portraits of \mathcal{H} in the cylinder \mathcal{C} , with compactified variables \bar{x} , \bar{y} and \bar{z} . The first column is for $\beta=0.3$ and the second column is for $\beta=-0.3$, and for each we present the two phase portraits for $\xi=1.8$ in the top row and $\xi=1.5$ in the bottom row. Each phase portrait shows the fixed points p^{\pm} with their one-dimensional stable manifolds $W^s(p^-)$ and $W^s(p^+)$, computed up to arclength of approximately 12,000 each. For simplicity, we plot only the outer layer of the two-dimensional manifold $W^u(p^-)$ or $W^u(p^+)$, which is the accessible boundary of the corresponding planar horseshoe; compare with Figure 3. These unstable manifolds were rendered as surfaces as the cross product between their planar counterparts $W^u(p_h^-)$ and $W^u(p_h^+)$, computed up to arclength approximately 9, and the line segment [-1,1] representing the \bar{z} -direction. Also shown is the hyperbolic set Λ , which we find as the intersection set of the computed stable manifolds with $W^u(p_h^\pm)$. The two circles represent the boundary of the cylinder \mathcal{C} , and they contain the sinks q^\pm and the saddle s^+ or s^- , respectively.

The one-dimensional stable manifolds $W^s(p^{\pm})$ in Figure 4 are 'spread out' in the \bar{z} -direction in an intricate way. They weave back and forth through the unstable manifolds $W^u(p^{\pm})$, creating the hyperbolic set Λ as the (closure of) their intersection set. Note that $W^s(p^-)$ and $W^s(p^+)$ accumulate on s^+ for $\beta = 0.3$ and on s^- for $\beta = -0.3$. Moreover, these two one-dimensional manifolds are completely intermingled, which is an illustration of the fact that the closure of each of them is $W^s(\Lambda)$. The hyperbolic set Λ itself is also spread out in the \bar{z} -direction, yet

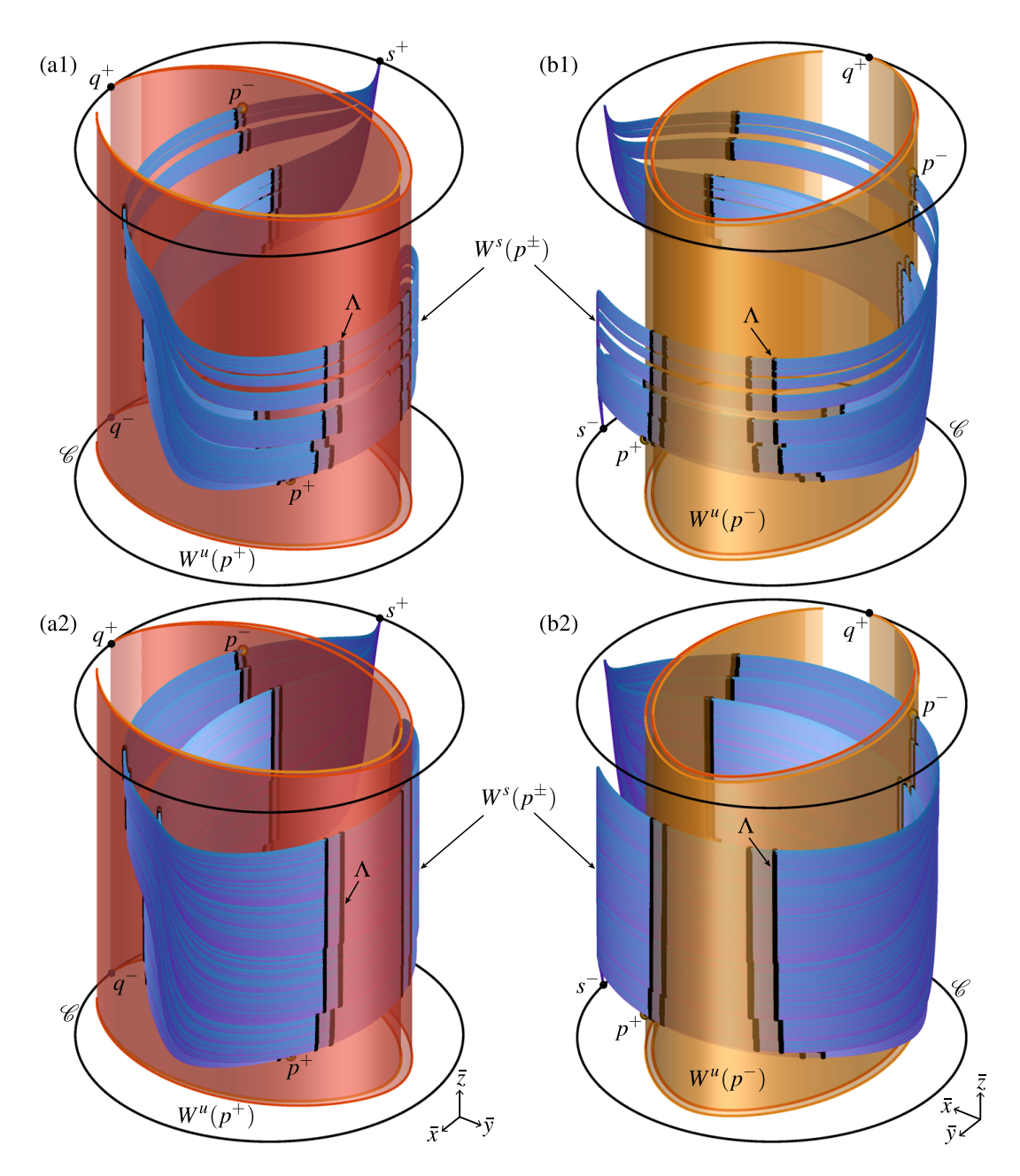


Figure 4: Phase portrait of \mathcal{H} in the cylinder \mathcal{C} for an orientation-preserving shear with $\xi > 1$. Panels (a1) and (a2) are for $\beta = 0.3$ with $\xi = 1.8$ and $\xi = 1.5$, respectively, and panels (b1) and (b2) for $\beta = -0.3$ with $\xi = 1.8$ and $\xi = 1.5$, respectively. Shown are the fixed points p^{\pm} (golden dots), the curves $W^s(p^-)$ (blue), $W^s(p^+)$ (purple), the surfaces $W^u(p^-)$ (red) and $W^u(p^+)$ (orange), the hyperbolic set Λ (black dots), and the points q^{\pm} and s^+ or s^- (black dots) on $\partial \mathcal{C}$.

projects down to the Cantor set Λ_h on the Poincaré disk \mathcal{D} ; the equivalent statement holds for the invariant manifolds. This is due to the skew-product structure of \mathcal{H} and, in fact, the top-down views of columns (a) and (b) are exactly panels (a2) and (b2) of Figure 3, respectively. We remark that the two cases shown in column (b) are very similar to those in [35, Fig. 2(a) and Fig. 3(a)], which are for $\alpha = 9.5$ and $\beta = -0.3$ in our formulation of \mathcal{H} .

Irrespective of the orientation properties of the underlying horseshoe, for $\xi = 1.8$ one observes in Fig 4(a1) and (b1) a structure of $W^s(p^{\pm})$ with distinct 'bands' and visible gaps between them.

For $\xi=1.5$ as in panels (a2) and (b2), on the other hand, there are no such gaps any longer and $W^s(p^\pm)$ give the impression of surfaces with several layers. It is important to emphasise that the curves $W^s(p^\pm)$ have been computed up to the same arclength in each case. While these images are suggestive, mere inspection is not sufficient to decide whether there is a blender or not. As we will show in subsequent sections, for either sign of $\beta=\pm 0.3$, the curves $W^s(p^\pm)$ do not have the carpet property and Λ is not a blender when $\xi=1.8$, while they do have the carpet property and, hence, Λ is a blender for $\xi=1.5$.

To come to this conclusion, we investigate the details of the transition to a blender as ξ is decreased from larger values. To this end, we consider the intersection points of the onedimensional manifolds with a half-plane Σ , which is chosen to provide a good separation of intersection points. For the orientation-preserving shear with $\xi > 1$, we choose

$$\Sigma := \{ (\bar{x}, \bar{y}, \bar{z}) \in \mathcal{C} \mid \bar{x} = 0 \text{ and } \bar{y} < 0 \}.$$
 (13)

We denote by $w^-(l;\xi)$ and $w^+(l;\xi)$ the l^{th} intersection of the curves $W^s(p^-)$ and $W^s(p^+)$ with Σ , respectively, for the chosen value of ξ . Here, $l \in \mathbb{Z} \setminus \{0\}$, where the sign of l distinguishes the two branches of the respective one-dimensional manifold and |l| enumerates the intersection points ordered along each arclength parametrised branch. For notational simplicity, we will refer to the intersection points $w^{\pm}(l;\xi)$ simply as $w^{\pm}(l)$ when ξ has a specific value. However, a key idea is to consider how the actual \bar{z} -coordinates of these enumerated intersection points change with ξ , which is why we define and study the ξ -parametrised curves of intersection points

$$\boldsymbol{w}^{\pm}(l) := \left\{ w^{\pm}(l;\xi) \mid \xi \in [\xi_a, \xi_b] \right\} \subset \Sigma \times [\xi_a, \xi_b]$$

for each l from a suitable index set $\mathcal{L} \subset \mathbb{Z} \setminus \{0\}$, where $[\xi_a, \xi_b]$ is a ξ -range of interest. For any chosen ξ -value, the ordered points $w^-(l;\xi)$ and $w^+(l;\xi)$ are found efficiently and accurately by the improved algorithm from [15] for computing long pieces of one-dimensional manifolds as arclength-parametrised curves. This enhanced capability enables us to compute the curves $\boldsymbol{w}^{\pm}(l)$ reliably by performing these calculations over a sufficiently fine mesh of ξ -values in $[\xi_a, \xi_b]$. By considering a suitable projection direction, one can check for which ξ -range the curves appear to be dense. More specifically, we consider throughout the projection onto the \bar{z} -axis in Σ , as in previous work [34, 35], which simply means that we plot the curves $\boldsymbol{w}^{\pm}(l)$ in the (ξ, \bar{z}) -plane. We now employ this general approach, starting with the two cases of orientation of \mathcal{H} with $\beta = \pm 0.3$ and $\xi > 1$.

3.1 Oriented horseshoe with $\xi > 1$

Figure 5 for $\alpha=4.2$ and $\beta=0.3$ sets the stage for the study of orientation-preserving \mathcal{H} with orientation-preserving h (and orientation-preserving shear) by considering the sufficiently large value $\xi=8.0$. Shown is how the stable manifolds $W^s(p^\pm)$ intersect the section Σ from (13) in the intersection sets $\{w^\pm(l)\}$. The situation is shown in panel (a1) in the three-dimensional cylinder, and the intersection sets $\{w^-(l)\}$ and $\{w^+(l)\}$ in Σ are shown in panel (a2); here and throughout, Σ is represented by its \bar{y} - and \bar{z} -coordinates. The top projection onto the Poincaré disk \mathcal{D} in panel (b1) and the 'side projection' onto the (\bar{x},\bar{z}) -plane in panel (c1), with the enlargements near Σ in panels (b2) and (c2), illustrate the structure of the manifolds $W^s(p^\pm)$ and associated sets of intersection points $\{w^\pm(l)\}$.

Recall that the structure of $W^s(p^{\pm})$ in projection onto \mathcal{D} is simply that of the oriented horseshoe of the Hénon map h discussed in Section 2.2; compare Figure 5(b1) with Figure 3(a2). Hence, the outer boundary and the boundaries of the gaps of the Cantor structure, of curves near Σ and of points in Σ , are formed by the accessible boundary $W^s(p^-)$ in panels (b1) and (b2). As panels (c1) and (c2) of Figure 5 illustrate, the projection of $W^s(p^{\pm}) \cap \Sigma$ onto the \bar{z} -axis is a Cantor set with exactly the same property: it has infinitely many gaps that are bounded by

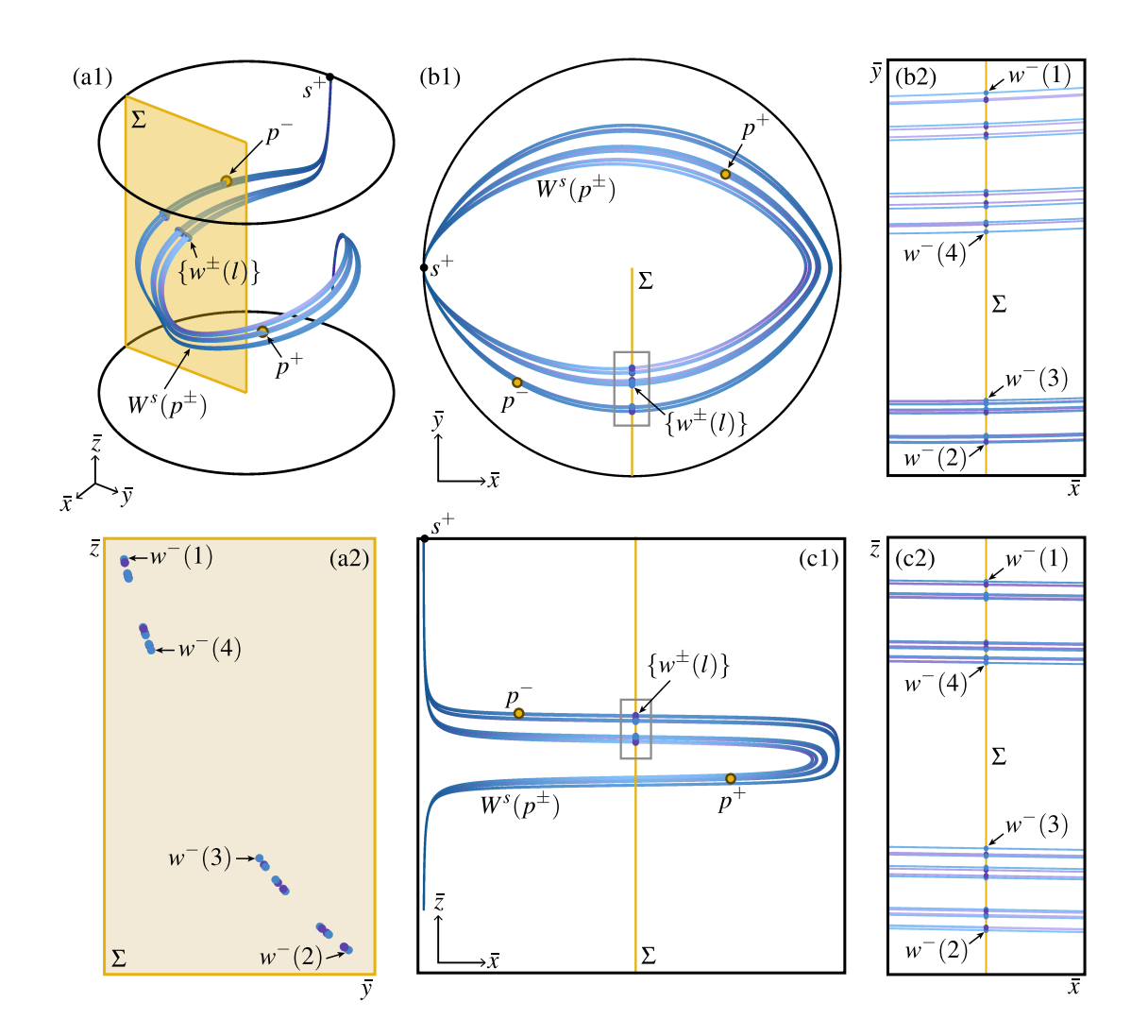


Figure 5: Illustration of the intersection sets $\{w^-(l)\}$ (blue) and $\{w^+(l)\}$ (purple) of the stable manifolds $W^s(p^-)$ (blue) and $W^s(p^+)$ (purple) of p^\pm (golden dots) with the section Σ (sand colour) for orientation-preserving h and orientation-preserving shear with $\xi=8.0$. Panel (a1) shows these objects in \mathcal{C} , and panel (a2) shows $\{w^\pm(l)\}$ in Σ . Panels (b1) and (c1) are projections onto the Poincaré disk \mathcal{C} and the (\bar{x},\bar{z}) -plane, respectively, which are enlarged near Σ in panels (b2) and (c2). The relevant branch of $W^s(p^-)$ is computed up to arclength 80, yielding $w^-(l)$ with $l \in \{1,\ldots,16\}$, and each branch of $W^s(p^+)$ is computed up to arclength 40, yielding $w^+(l)$ with $l \in \{-8,\ldots,-1\} \cup \{1,\ldots,8\}$. Here, $\alpha=4.2$ and $\beta=0.3$.

points in $\{w^-(l)\}$. Moreover, Figure 5(a2) suggests that the Cantor set $W^s(p^\pm) \cap \Sigma$ lies on the graph of a smooth, monotonically decreasing function from \bar{y} to \bar{z} . This can be interpreted as numerical evidence that the hyperbolic set $\Lambda \subset \mathbb{R}^3$ lies in a normally hyperbolic smooth two-dimensional submanifold when $\xi = 8.0$. In particular, $W^s(\Lambda)$ does not have the carpet property when seen in projection along any C^1 -smooth curves and, hence, Λ is not a blender.

Figure 6 shows how $W^s(p^{\pm}) \cap \Sigma$ changes as ξ is decreased. While its Cantor structure in projection along the \bar{z} -direction (onto the horizontal \bar{y} -axis in the panels) remains unchanged, the projection onto the (vertical) \bar{z} -axis undergoes some pretty dramatic changes. To illustrate this further, we label the intersection points that bound the projection onto the \bar{z} -axis and the bounding intersection points of its main gap Δ_1 , and we highlight $w^-(3)$ and $w^-(4)$.

Figure 6(a) for $\xi = 6.0$ is topologically and geometrically as Figure 5(a2) for $\xi = 8.0$, with the points in $W^s(p^{\pm}) \cap \Sigma$ still apparently lying on the graph of a monotonically decreasing function.

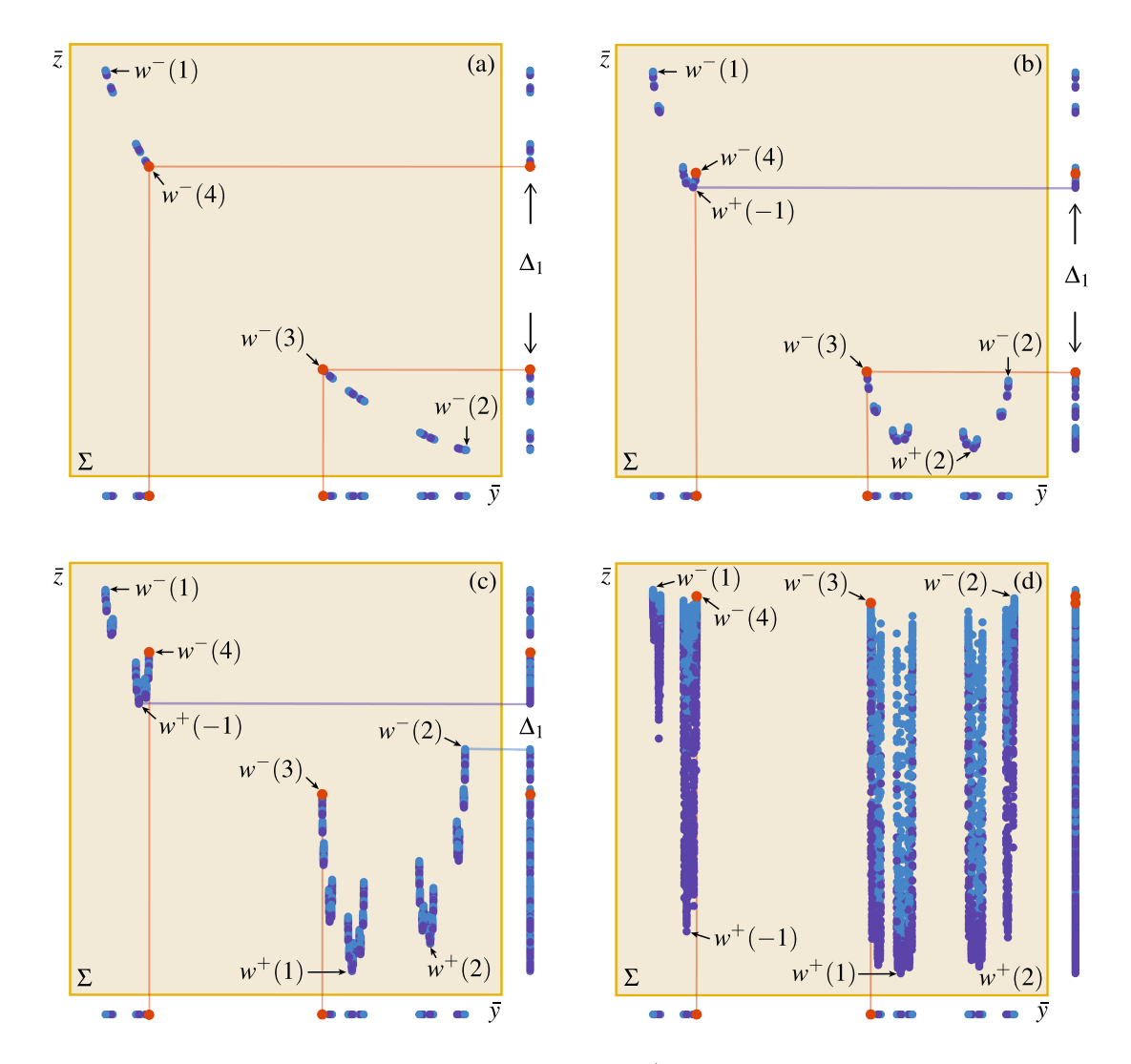


Figure 6: Intersection sets $\{w^-(l)\}$ (blue dots) and $\{w^+(l)\}$ (purple dots) in Σ and in projection onto the \bar{y} - and \bar{z} -axes, for $\xi=6.0$ (a), $\xi=2.5$ (b) , $\xi=1.8$ (c), and $\xi=1.2$ } (d). There are 2^{10} points in each intersection set; labelled are the outermost intersection points and those bounding the main gap Δ_1 in projection onto the \bar{z} -axes, while $w^-(3)$ and $w^-(4)$ are highlighted in red. Here $\alpha=4.2$ and $\beta=0.3$.

When ξ is reduced to $\xi=2.5$, as in Figure 6(b), this is no longer the case: the points of $\{w^{\pm}(l)\}$ are now arranged in groups in what appear to be 'nested U-shapes'. In particular, the lower minimum intersection point with respect to the \bar{z} -coordinate is now the point $w^+(2)$ instead of $w^-(2)$; similarly, the upper boundary of the main gap Δ_1 is now $w^+(-1)$ instead of $w^-(4)$. In fact, there is a change in the upper boundary of all gaps: these are now defined by the minimum points of the respective U-shapes. When ξ is reduced further to $\xi=1.8$, as in panel (c), there is also a change of the lower boundary of Δ_1 : it is no longer $w^-(3)$ but the top-right point of the corresponding U-shape, which is actually the point $w^-(2)$; similarly, $w^-(4)$ is now the lower boundary of the next biggest gap above Δ_1 . Note also that the global extremal points are $w^-(1)$ and $w^+(1)$, meaning that the global minimum has changed again. It is not clear whether the projection of $W^s(p^\pm)\cap\Sigma$ onto the the \bar{z} -axis is dense for $\xi=1.8$; see also Figure 4(a1). However, for the even lower value of $\xi=1.2$, as in Figure 6(d), this projection does not appear to have any gaps. This is evidence that $W^s(\Lambda)$ has the carpet property and, hence, Λ is a blender. Note that the points $w^-(3)$ and $w^-(4)$ are now very much near the top boundary of this projection.

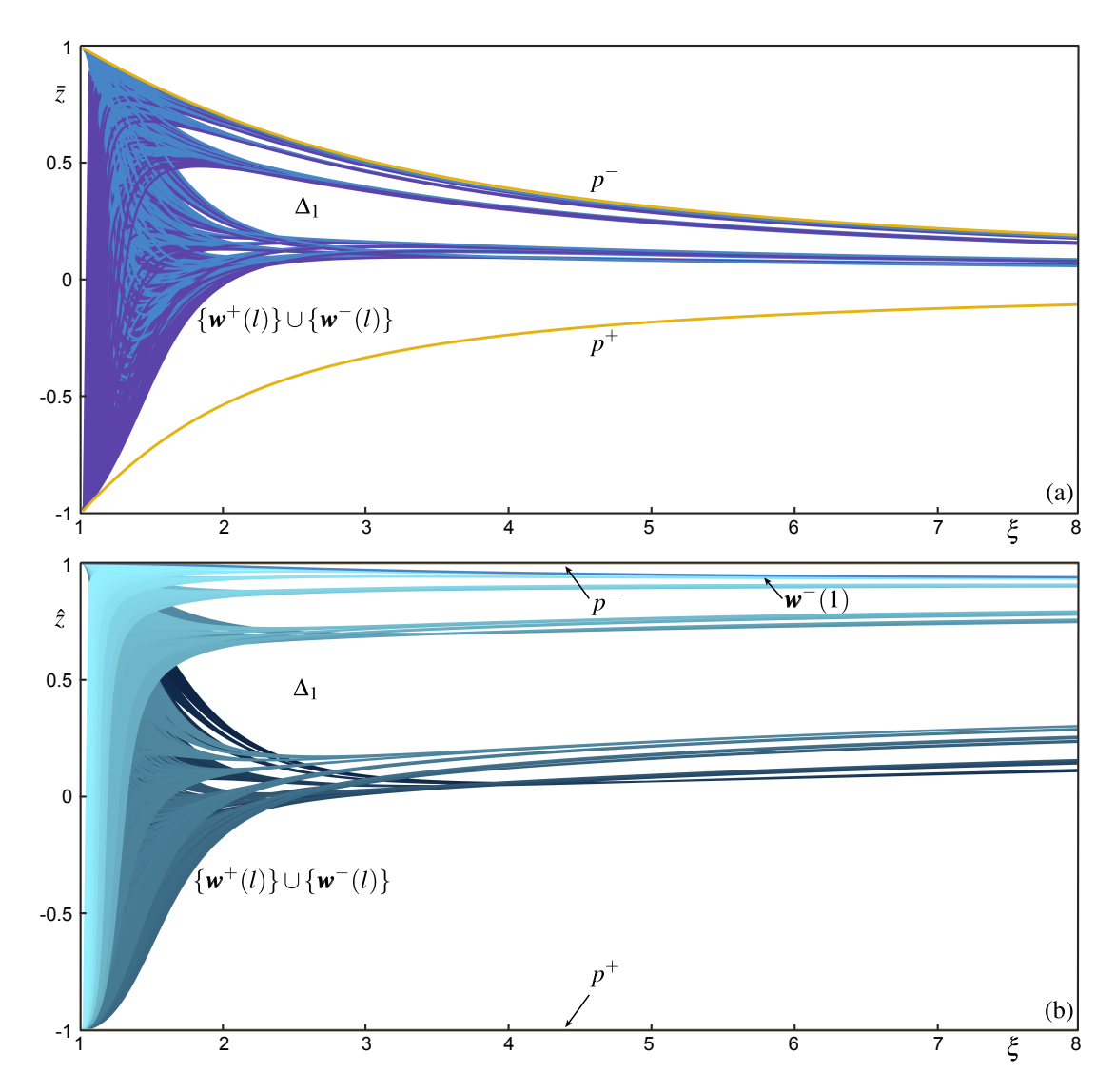


Figure 7: The fixed points p^{\pm} (yellow curves) and 2^{11} computed curves each of the sets $\{\boldsymbol{w}^{\pm}(l)\}$ for $\alpha=4.2$ and $\beta=0.3$ with $\xi\in[1.02,8]$; the main gap Δ_1 is labelled. Panel (a) shows $\{\boldsymbol{w}^{-}(l)\}$ (blue) and $\{\boldsymbol{w}^{+}(l)\}$ (purple) in projection onto the (ξ,\bar{z}) -plane; in panel (b) these curves are coloured from dark to light cyan based on their \bar{y} -coordinates and shown in the rescaled (ξ,\hat{z}) -plane where p^{\pm} lie at ± 1 .

3.1.1 The carpet of carpets for $\beta > 0$ with $\xi > 1$

We obtain a better understanding of the reorganisation of intersection points in projection onto the \bar{z} -axis as ξ varies by considering the ξ -parametrised curves $\{\boldsymbol{w}^{\pm}(l)\}$ over the ξ -range [1.02, 8]. Specifically, Figure 7 shows $\{\boldsymbol{w}^{-}(l)\}$ for $1 \leq l \leq 2^{11}$ and $\{\boldsymbol{w}^{+}(\pm l)\}$ for $1 \leq l \leq 2^{10}$, which were found by computing the respective sequentially ordered intersection points over this ξ -range in steps of 0.02. The main gap Δ_1 is labelled, and also shown are the ξ -parametrised \bar{z} -values of the fixed points p^{-} and p^{+} , as given by (10).

Figure 7(a) shows the (ξ, \bar{z}) -plane with $\{w^-(l)\}$ in blue and $\{w^+(l)\}$ in purple; the four projections onto the \bar{z} -axis in Figure 6 are found as intersections with vertical lines for the respective values of ξ . Note that the curves in $\{w^\pm(l)\}$ are all bounded in their \bar{z} -range by p^- and p^+ . For large ξ -values, the curves in $\{w^-(l)\}$ exhibit clear gaps, which are homeomorphic images of the gaps of the Cantor set associated with the oriented horseshoe with accessible

boundary $W^s(p_h^-)$. As ξ is decreased, the curves eventually begin to cross, which leads to changes in the boundary of Δ_1 and all other gaps. The gaps then close as ξ is decreased further and the shown curves appear to fill a solid region for ξ -values close to 1, which is evidence that Λ has the carpet property. We also refer to this representation as the *carpet of carpets*.

Note the small range of \bar{z} -values between p^- and p^+ for intermediate to large values of ξ , which makes it difficult to discern the organisation of the curves. For this reason, and from now, we rescale \bar{z} to the coordinate denoted \hat{z} given by the linear transformation that maps the \bar{z} -value of p^- to $\hat{z}=1$ and that of p^+ to $\hat{z}=-1$. Figure 7(b) shows the resulting image in the (ξ,\hat{z}) -plane, where we now colour the curves from dark to light cyan in a gradient based on their respective \bar{y} -values (which do not change with ξ); note that the upper boundary curve is $\{w^-(1)\}$ throughout, in agreement with Figure 6. The representation in Figure 7(b) illustrates how intersection curves cross and change relative positions when ξ is reduced towards $\xi=1.0$. The colour gradient agrees with the \hat{z} -value for large ξ , since the two projections onto the \bar{y} -axis and the \bar{z} - or \hat{z} -axis are topologically the same Cantor set. However, this is no longer the case when curves in $\{w^{\pm}(l)\}$ have crossed for lower values of ξ . Notice, in particular, the intricate re-arrangement of the curves below the main gap Δ_1 . In what may be called informally a 'recursive twisting' of their relative positions in the (\bar{y}, \bar{z}) -plane, the lower extremal boundary of all intersection points becomes the lower boundary of Δ_1 when ξ is decreased; this corresponds to the development of 'nested U-shapes' seen in the panels of Figure 6.

3.1.2 The boundary curves of the relevant gaps for $\beta > 0$ with $\xi > 1$

We find that the phenomenon of changing boundaries of gaps — via the appearance of nested U-shapes — is a precursor to all gaps closing and, hence, an important ingredient in the process of Λ becoming a blender. As was previously observed in [34, 35, 36], the gaps Δ_i that determine the creation of a blender are the largest gaps in the Cantor structure with \hat{z} -values above the main (and largest) gap Δ_1 ; note that the gaps Δ_j accumulate on the top-most curve $\boldsymbol{w}^-(1)$. In terms of the Cantor structure of $W^s(\Lambda_h)$ of the underlying planar Hénon map, Δ_1 has \bar{y} values around 0 and is the gap at level 1 of the Cantor construction; Δ_j is the 'left gap' at each subsequent level, that is, the one with the lower \bar{y} -value; see Figure 6(a)–(c). Figure 8 shows which of the curves in $\{w^{\pm}(l)\}$ bound the respective gap Δ_j for which ranges of ξ . Panel (a) shows the (ξ, \hat{z}) -plane from Figure 7(b), but now all computed curves in $\{w^{\pm}(l)\}$ colored grey, except for the top-most curve $\{w^{-}(1)\}\$ and the specific curves that bound Δ_1 to Δ_6 , which are in shades of brown, green, blue, red, purple and yellow, respectively. The region in the frame, near where the gaps Δ_i close, is enlarged in panel (b). We mark particular points on these curves. The points c_i indicate where Δ_1 to Δ_6 (of which the first two are labelled) close. The points labelled s_i are switching points, where there is a crossing of two specific curves resulting in a change of the curve that forms the bottom boundary of Δ_i ; the points labelled b_i and e_i mark the beginning and end of a ξ -range of many crossings of curves that form the top boundary of Δ_i . The two insets of Figure 8(a) illustrate further how the bottom and top boundaries of these first six gaps change, by showing the respective indices |l| as a function of ξ .

Figure 8 shows that the bottom boundary of Δ_1 is determined by only two different curves: for large ξ , it is $\mathbf{w}^-(3)$ (gold) and, as ξ is decreased, it switches at s_1 to $\mathbf{w}^-(2)$ (brown). The equivalent statement is true for the upper boundaries of all other gaps Δ_j . As the enlargement in panel (b) illustrates, the bottom boundary of Δ_2 is $\mathbf{w}^-(5)$ for larger values of ξ and $\mathbf{w}^-(4)$ for ξ below the point s_2 . Moreover, the left inset of Figure 8(a) shows that the bottom boundaries of Δ_3 to Δ_6 correspond to two distinct indices with a single switch at the point s_j . Note that all bottom boundary curves of the gaps Δ_j are curves in $\{\mathbf{w}^-(l)\}$.

The top boundary of the gaps Δ_j involves more complicated changes. For large ξ in Figure 8(a), the top boundary of Δ_1 is the intersection curve $\mathbf{w}^-(4)$ (green). Panel (b) shows

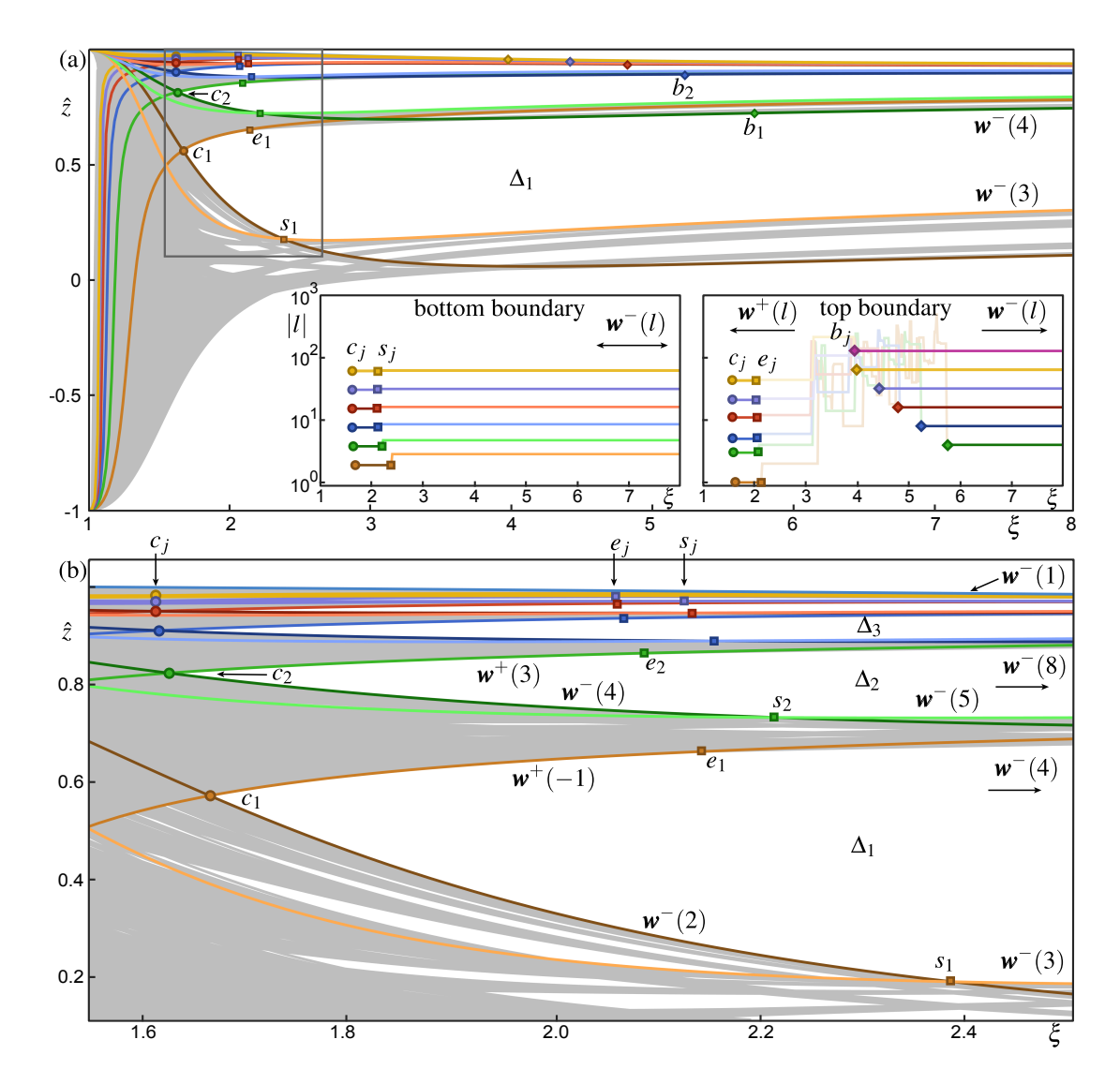


Figure 8: Boundary curves of the gaps Δ_1 to Δ_6 in the (ξ, \hat{z}) -plane for $\alpha = 4.2$ and $\beta = 0.3$, overlaid in colour onto $\{\boldsymbol{w}^{\pm}(l)\}$ (grey) from Figure 7(b). Also labelled are the closing points c_j , switching points s_j , and the begin and end points b_j and e_j that bound the ξ -range of crossing curves. Panel (a) is over the range $\xi \in (1, 8]$, and its inset shows the corresponding modulus of the indices |l| versus ξ for the bottom and top boundaries of Δ_j , respectively. Panel (b) is an enlargement of the shown frame in panel (a) around where the gaps Δ_j close.

that, when ξ is sufficiently small this top boundary is $\mathbf{w}^+(-2)$ (light gold), which is associated with $W^s(p^+)$. Similarly, for large ξ the top boundary of Δ_2 is $\mathbf{w}^-(8)$ (blue), while for small ξ it is $\mathbf{w}^+(3)$ (green). The right inset shows that the top boundaries of Δ_1 to Δ_6 involve a complex transition that begins at the points b_j and ends at e_j (as ξ is decreased). Between these two points, there is no single index |l| that exclusively defines the boundary of Δ_j . Instead, numerous different indices |l| associated with both $W^s(p^-)$ and $W^s(p^+)$ are found in our computations. This transition manifests itself as the 'recursive twisting' phenomenon we observed in Figure 7(b) with the corresponding emergence of U-shapes in Figure 6 — and we associate it with the loss of normal hyperbolicity of a two-dimensional smooth submanifold in which the horseshoe (supposedly) lies for sufficiently large ξ ; see [2] for a similar argument.

Note in Figure 8 that the point c_j has a lower ξ -value than the points s_j and e_j , whose ξ -values are listed for $1 \leq j \leq 9$ in Table 6 in the Appendix. Hence, an important conclusion is

Closing of the gaps Δ_j for $\xi > 1$ and $\beta = 0.3$

| | boundin | bounding curves | | ξ -value of c_j | | | | |
|---------------|-------------------|-------------------|--|-----------------------|---------------|---------|--|--|
| j | $c_j < \xi < s_j$ | $c_j < \xi < e_j$ | | ξ_j | d_{j} | r_{j} | | |
| 1 | $w^{-}(2)$ | $w^+(-1)$ | | 1.666870 | | | | |
| $\mid 2 \mid$ | $ w^{-}(4) $ | $w^{+}(3)$ | | 1.627446 | 0.039424 | | | |
| 3 | $w^{-}(8)$ | $w^{+}(-5)$ | | 1.617546 | 0.009900 | 0.2511 | | |
| $\mid 4 \mid$ | $w^{-}(16)$ | $ w^{+}(11) $ | | 1.614701 | 0.002845 | 0.2874 | | |
| 5 | $w^{-}(32)$ | $w^+(-21)$ | | 1.613875 | 0.000825 | 0.2901 | | |
| 6 | $w^{-}(64)$ | $w^{+}(43)$ | | 1.613636 | 0.000240 | 0.2904 | | |
| 7 | $w^{-}(128)$ | $w^{+}(-85)$ | | 1.613566 | 0.000070 | 0.2907 | | |
| 8 | $w^{-}(256)$ | $w^{+}(171)$ | | 1.613546 | 0.000020 | 0.2908 | | |
| 9 | $w^{-}(512)$ | $ w^{+}(-341) $ | | 1.613540 | 0.000006 | 0.2907 | | |
| | | | | 1.613537 | $pprox \xi^*$ | | | |

Table 2: Curves from $\{\boldsymbol{w}^-(l)\}$ and $\{\boldsymbol{w}^+(l)\}$ that form the boundaries of Δ_j near the closing points c_j for $\xi > 1$ and $\beta = 0.3$ (left block), and computed ξ_j -values of c_j with consecutive differences $d_j = |\xi_j - \xi_{j-1}|$ and contraction rates $r_j = d_j/d_{j-1}$ (right block); also shown is the resulting limit ξ^* .

that there are definite intersection curves that form the bottom and top boundaries of Δ_j near the point c_j where the gap closes. We are able to identify these two boundary curves in $\{\boldsymbol{w}^{\pm}(l)\}$, formed by $W^s(p^-)$ for the bottom and $W^s(p^+)$ for the top boundary, by the respective index l for $1 \leq j \leq 9$. This data is presented in the left block of Table 2, and it allows us to conclude that the indices of the bottom and top boundaries $\boldsymbol{w}^-(a_j^b)$ and $\boldsymbol{w}^+(a_j^t)$ of the gaps Δ_j satisfy the recurrence relations

$$\begin{cases} a_{j+1}^b = 2a_j^b & \text{with } a_1^b = 2, \\ a_{j+1}^t = -2a_j^t + 1 & \text{with } a_1^t = -1. \end{cases}$$
 (14)

Moreover, the sequences (a_i^b) and $(|a_i^t|)$ satisfy the same two-stage recursion

$$R_k = R_{k-1} + 2R_{k-2}$$
 with
$$\begin{cases} R_1 = 2, \ R_2 = 4 & \text{for } (a_j^b), \\ R_1 = 1, \ R_2 = 3 & \text{for } (|a_i^t|), \end{cases}$$

which identifies them as Lucas sequences [6]. Specifically, $a_j^b = 2^j$ and $|a_j^t| = J_{j+1}$ are the Jacobsthal numbers [39], which can be expressed explicitly as

$$J_j := \frac{2^j - (-1)^j}{3}.$$

Hence, the two boundaries of Δ_j near c_j are given by

$$\mathbf{w}^{-}(2^{j})$$
 and $\mathbf{w}^{+}((-1)^{j}J_{j+1})$. (15)

We find the secondary recurrence relation $a_{j+2}^t = 4a_j^t - 1$ under \mathcal{H}^2 , which maps each branch of the nonoriented manifold $W^s(p^+)$ to itself; similarly, we trivially have $a_{j+2}^b = 4a_j^b$. Furthermore, the odd and even subsequences of both (a_j^b) and (a_j^t) from (14) are also Lucas sequences, with the recurrence

$$R_k = 5R_{k-1} - 4R_{k-2},\tag{16}$$

where the respective first and third, and second and fourth indices in Table 2 are the seeds R_1 and R_2 .

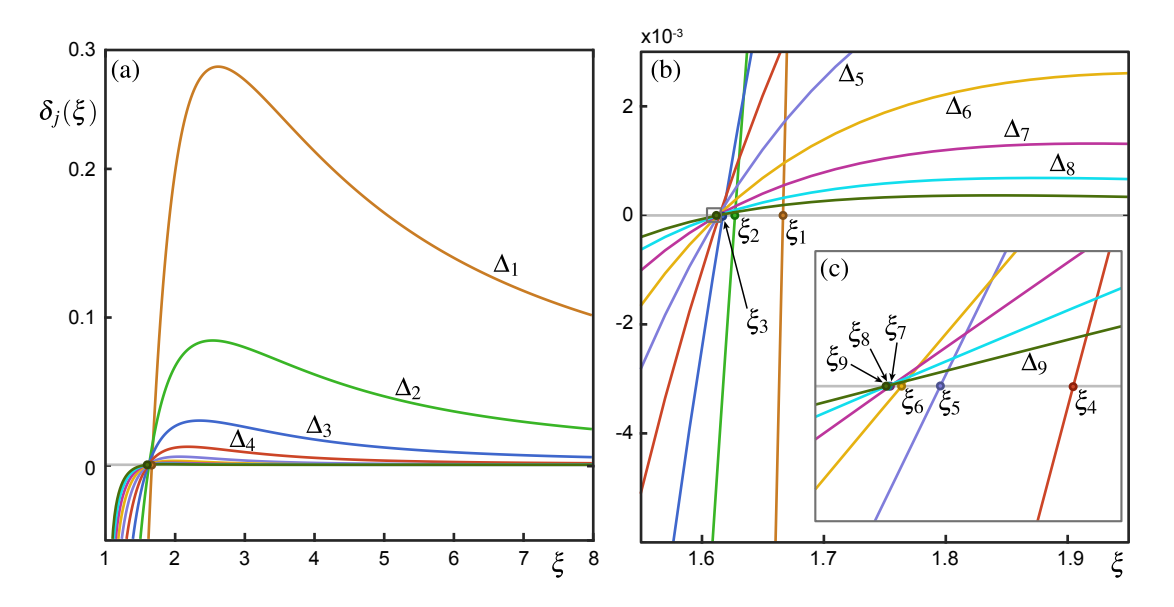


Figure 9: The signed difference functions $\delta_j(\xi)$ for $\alpha = 4.2$ and $\beta = 0.3$ of the gaps Δ_j for j = 1, ..., 9 with $\xi > 1$. Panel (a) shows them for $\xi \in (1, 8]$, and panels (b) and (c) are successive enlargements near the zeros ξ_j .

3.1.3 The limit of the closing points c_j for $\beta > 0$ with $\xi > 1$

The identification of the two bounding curves near c_j in terms of the index l of $\mathbf{w}^-(l)$ and $\mathbf{w}^+(l)$, as given in the left block of Table 2 and by (15), constitutes interesting topological information. In particular, it allows us to compute in an efficient way when the gap Δ_j closes by considering the signed differences $\delta_j(\xi)$ between the \hat{z} -values of these respective two intersection curves; note that $\delta_j(\xi) < 0$ when Δ_j has closed. It is a major advantage that the indices involved are surprisingly low, and this allows us to determine the ξ -value ξ_j of c_j very accurately as a regular zero of $\delta_j(\xi)$.

Figure 9 shows the graphs of the difference functions $\delta_j(\xi)$ of the gaps Δ_j for $1 \leq j \leq 9$ near their respective zeros ξ_j . Panel (a) shows the full ξ -range (1,8], and the successive enlargements in panels (b) and (c) illustrate that the gaps Δ_j close one after the other as ξ is decreases, that is, $\xi_{j+1} < \xi_j$. Moreover, the values ξ_j are all very close to one another and show fast convergence to a limiting value ξ^* . In order to obtain the values ξ_j accurately, we find the values of $\delta_j(\xi)$ on a finer mesh of stepsize 0.004 over the range [1.61, 1.67], and use local cubic spline interpolation through this data to compute the respective zeros. The right block of Table 2 shows the computed values of ξ_j for the first nine gaps Δ_j , together with the consecutive differences $d_j = |\xi_j - \xi_{j-1}|$ and the contraction rates $r_j = d_j/d_{j-1}$. From this data, we obtain the estimate $\xi^* \approx 1.613537$ for the limit of the ξ_j , which are indeed seen to converge fast. In particular, the r_j stabilise to within the accuracy of their computation of about 10^{-3} , and this is evidence that the convergence of the ξ_j is geometric in the limit. Therefore, we have confidence in the statement that Λ has the carpet property and is a blender for any ξ -value below 1.613537.

3.2 Nonoriented horseshoe with $\xi > 1$

We now investigate the transition to a blender when both h and \mathcal{H} are orientation reversing. To this end, we change the sign of β , so $\beta = -0.3$, and keep $\alpha = 4.2$ unchanged; hence, h has the nonoriented full horseshoe shown in Figure 3(b).

Figure 10 shows the computed intersection sets $W^s(p^{\pm}) \cap \Sigma$, for $\xi = 6.0$ in panel (a) and for $\xi = 2.5$ in panel (b). Comparison with panels (a) and (b) of Figure 6 reveals considerable

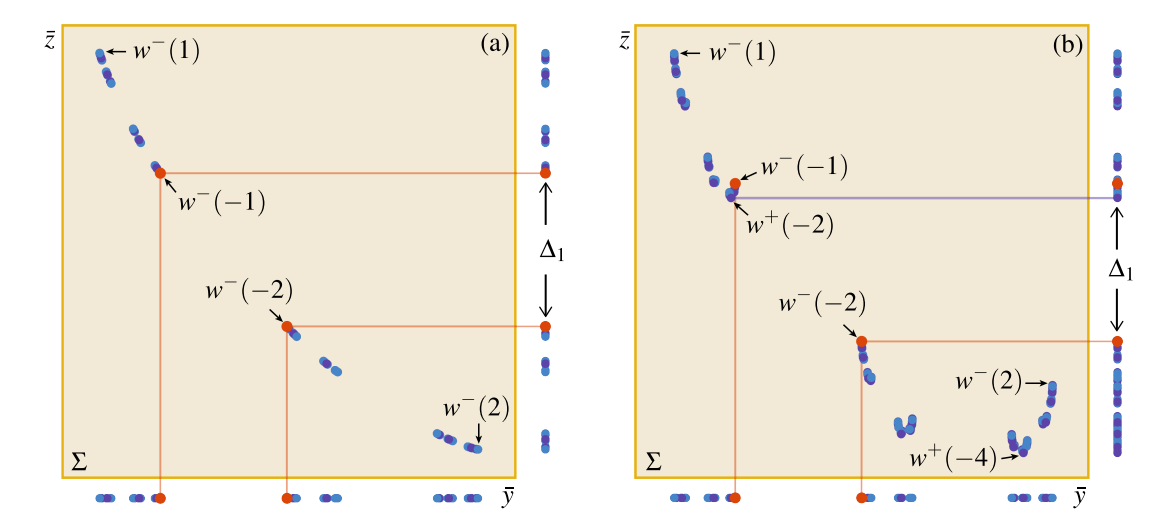


Figure 10: Intersection sets $\{w^-(l)\}$ (blue dots) and $\{w^+(l)\}$ (purple dots) in Σ and in projection onto the \bar{y} - and \bar{z} -axes, for $\xi=6.0$ (a) and $\xi=2.5$ (b). There are 2^{10} points in each intersection set; labelled are the outermost intersection points and those bounding the main gap Δ_1 in projection onto the \bar{z} -axes, while $w^-(-1)$ and $w^-(-2)$ are highlighted in red. Here, $\alpha=4.2$ and $\beta=-0.3$.

similarities but also differences. The intersection set $\{w^{\pm}(l)\}\subset\Sigma$ for $\xi=6.0$ in Figure 10(a) also appears to lie on the graph of a monotonically decreasing function, so that its two projections onto the \bar{y} - and the \bar{z} -axis are homeomorphic. This is no longer the case in panel (b) for $\xi=2.5$, where there are again U-shapes of intersection points, with their local extrema as boundary points of the gaps Δ_j . On the other hand, while $W^s(p_h^-)$ is still the accessible boundary, this manifold is now nonoriented, which leads to different — and also negative — indices l for the boundary points in $\{w^-(l)\}$ in $W^s(p^-)$. The outer points are actually still $w^-(1)$ and $w^-(2)$, but the projection onto the \bar{y} -axis of the main gap Δ_1 is now bounded by $w^-(-1)$ and $w^-(-2)$; indeed, this agrees with the sketch in Figure 3(b1). Note also that the lowest points of the U-shapes in Figure 10 are still $\{w^+(l)\}$ but, since $W^s(p^+)$ is now oriented, their indices l all have the same sign.

Figure 11 shows how the corresponding curves in $\{\boldsymbol{w}^-(l)\}$ and $\{\boldsymbol{w}^+(l)\}$ cross and change roles; this figure has the exact same layout as Figure 8, with $\{\boldsymbol{w}^-(l)\}$ in grey and indvidual curves coloured if they bound gaps. The overall structure is the same: the relevant gaps Δ_j are again the ones including and above the main gap Δ_1 . Moreover, there is a single crossing point s_j of two boundary curves for the bottom boundary of each gap Δ_j , and begin and end points b_j and e_j of a region with many crossing curves for the top boundary of Δ_j . Comparison of the insets in panel (a) of Figures 11 and 8 shows that the points s_j and e_j now lie closer to where Δ_j closes. Nevertheless, the closing points c_j still have lower ξ -value than the points s_j and e_j (see Table 7 in the Appendix), and so the points c_j are again given by curves in $\{\boldsymbol{w}^-(l)\}$ and $\{\boldsymbol{w}^+(l)\}$, respectively, with specific indices l as shown in Figure 11(a).

The boundaries of Δ_j near c_j for $1 \leq j \leq 9$ are listed in the left block of Table 3. The respective indices do not follow the same pattern we found for positive β in Section 3.1; instead, the Jacobsthal numbers are now involved for both boundaries. Specifically, we find that the bottom and top boundaries $\boldsymbol{w}^-(a_j^b)$ and $\boldsymbol{w}^+(a_j^t)$ of the gaps Δ_j near c_j are determined by the recurrence relations

$$\begin{cases}
 a_{j+1}^b = -2(a_j^b - 1) + \mathbf{1}_2(j+1) & \text{with } a_1^b = 2, \\
 a_{j+1}^t = 2a_j^t + \mathbf{1}_2(j+1) & \text{with } a_1^t = -2,
\end{cases}$$
(17)

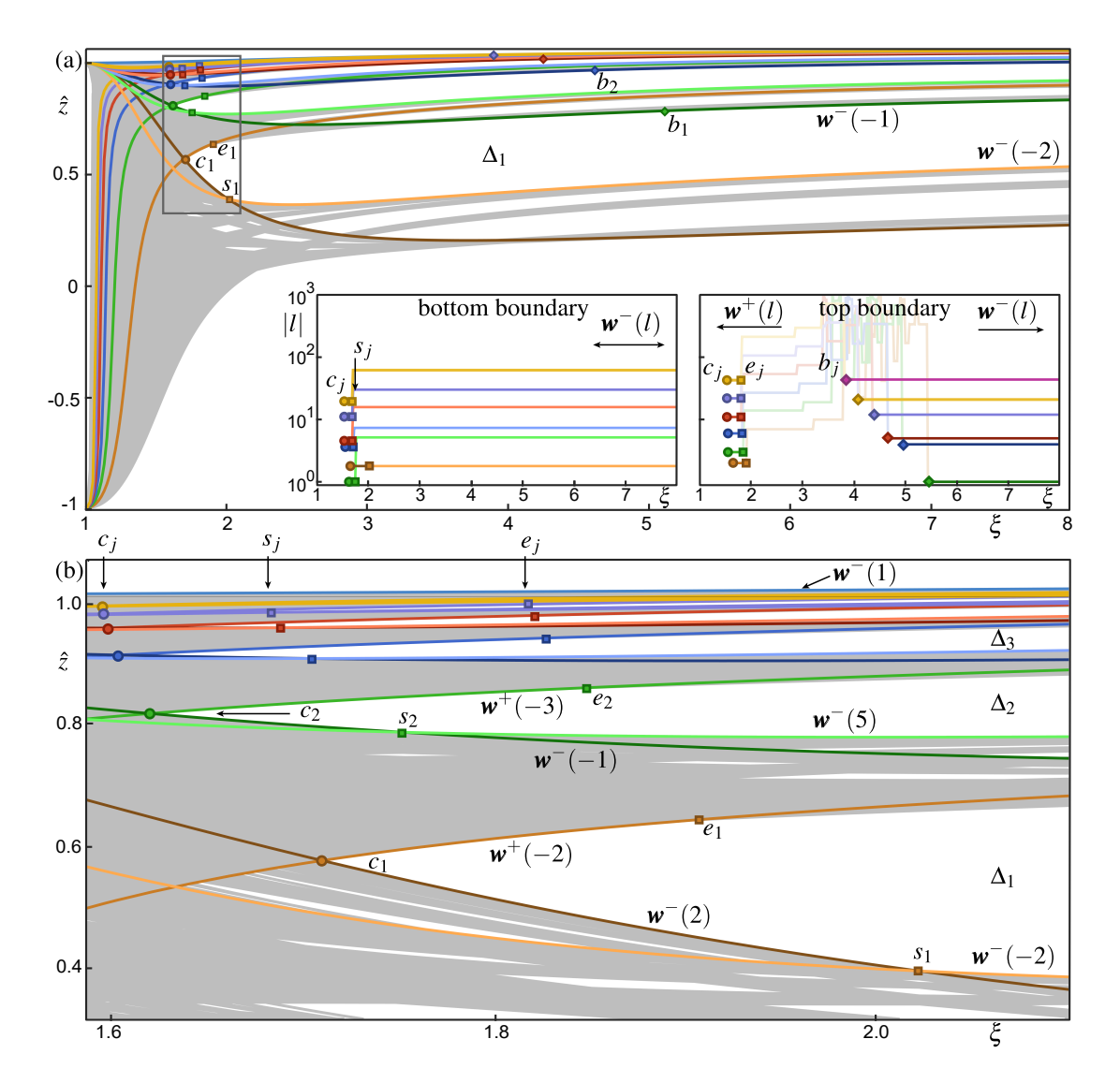


Figure 11: Boundary curves of the gaps Δ_1 to Δ_6 in the (ξ, \hat{z}) -plane for $\alpha = 4.2$ and $\beta = -0.3$, overlaid in colour onto $\{\boldsymbol{w}^{\pm}(l)\}$ (grey). Also labelled are the closing points c_j , switching points s_j , and the begin and end points b_j and e_j that bound the ξ -range of crossing curves. Panel (a) is over the range $\xi \in (1, 8]$, and its inset shows the corresponding modulus of the indices |l| versus ξ for the bottom and top boundaries of Δ_j , respectively. Panel (b) is an enlargement of the shown frame in panel (a) around where the gaps Δ_j close. Compare with Figure 8.

where

$$\mathbf{1}_{k}(n) := \begin{cases} 1, & \text{if } k \text{ divides } n, \\ 0, & \text{otherwise,} \end{cases}$$
 (18)

is an indicator function of divisibility by k; in particular, $\mathbf{1}_2(n)$ distinguishes whether n is even or odd. The recurrences (17) can be solved to give the bottom and top boundaries of Δ_j near c_j , respectively, as

$$w^-((-1)^{j+1}J_j + \mathbf{1}_2(j+1))$$
 and $w^+(-(J_{j+1} + \mathbf{1}_2(j+1))).$

As in Section 3.1.2, we also find secondary recurrence relations for \mathcal{H}^2 . For the bottom boundary generated by the nonoriented manifold $W^s(p^-)$ we have

$$a_{j+2}^b = 4a_j^b + \begin{cases} -4, & \text{if } j \text{ is odd,} \\ -1, & \text{if } j \text{ is even,} \end{cases}$$

Closing of gaps Δ_j for $\xi > 1$ and $\beta = -0.3$

| | bounding curves | | ξ -value of c_j | | | |
|---------------|-------------------|-------------------|-----------------------|----------|---------------|--------|
| $\mid j \mid$ | $c_j < \xi < s_j$ | $c_j < \xi < e_j$ | | ξ_j | d_{j} | r_j |
| 1 | $w^{-}(2)$ | $w^+(-2)$ | | 1.708510 | | |
| 2 | $ w^{-}(-1) $ | $w^{+}(-3)$ | | 1.618278 | 0.090232 | |
| 3 | $w^{-}(4)$ | $ w^+(-6) $ | | 1.601710 | 0.016568 | 0.1836 |
| $\mid 4 \mid$ | $w^{-}(-5)$ | $ w^+(-11) $ | | 1.596065 | 0.005645 | 0.3406 |
| 5 | $w^{-}(12)$ | $w^{+}(-22)$ | | 1.594324 | 0.001741 | 0.3084 |
| 6 | $w^{-}(-21)$ | $w^{+}(-43)$ | | 1.593764 | 0.000561 | 0.3219 |
| 7 | $w^{-}(44)$ | $w^{+}(-86)$ | | 1.593583 | 0.000181 | 0.3226 |
| 8 | $w^{-}(-85)$ | $ w^{+}(-171) $ | | 1.593524 | 0.000059 | 0.3235 |
| 9 | $w^{-}(172)$ | $ w^{+}(-342) $ | | 1.593505 | 0.000019 | 0.3236 |
| ∞ | | | | 1.593501 | $pprox \xi^*$ | |

Table 3: Curves from $\{\boldsymbol{w}^-(l)\}$ and $\{\boldsymbol{w}^+(l)\}$ that form the boundaries of Δ_j near the closing points c_j for $\xi > 1$ and $\beta = -0.3$ (left block), and computed ξ_j -values of c_j with consecutive differences $d_j = |\xi_j - \xi_{j-1}|$ and contraction rates $r_j = d_j/d_{j-1}$ (right block); also shown is the resulting limit ξ^* .

and for the top boundary generated by the oriented $W^{s}(p^{+})$ we have

$$a_{j+2}^t = 4a_j^t + \begin{cases} 2, & \text{if } j \text{ is odd,} \\ 1, & \text{if } j \text{ is even.} \end{cases}$$

Both sequences (a_i^b) and (a_i^t) satisfy the recurrence

$$R_k = -R_{k-1} + 2R_{k-2} + (-1)^k,$$

which means that they are not Lucas sequences [6] (because they satisfy recurrences with an additional alternating term). However, their secondary odd and even subsequences are Lucas sequences and, in fact, satisfy the recurrence (16) from Section 3.1.2, with the respective first two odd and even indices from Table 3 as the seeds R_1 and R_2 .

We use this information to define the signed difference functions $\delta_j(\xi)$ for the gaps Δ_j for this case; they are shown in Figure 12 for Δ_1 up to Δ_9 . This figure is very similar to Figure 9: again, $\xi_{j+1} < \xi_j$ and the zeros ξ_j converge fast. The values for $1 \le j \le 9$, computed by spline interpolation from data over the ξ -range [1.59, 1.71] in steps of 0.004, are listed in the right block of Table 3 with the consecutive differences d_j and contraction rates r_j . This data shows that the sequence ξ_j is also effectively geometric and has the limit $\xi^* \approx 1.593501$ below which all gaps have closed and Λ is a blender.

4 Transition to a blender for an orientation-reversing shear

When ξ is negative the Hénon-like map \mathcal{H} is orientation reversing on the z-fibres. We speak of an orientation-reversing shear and consider $\xi < -1$, so that the stable manifold $W^s(\Lambda)$ of the hyperbolic set Λ is again of dimension one. We then proceed as in the previous section and investigate the two cases of an oriented and a nonoriented horseshoe of the Hénon map h for $\beta = 0.3$ and $\beta = -0.3$ in Sections 4.1 and 4.2, respectively.

A new feature is that \mathcal{H} is now orientation reversing for positive and orientation preserving for negative β . More importantly, we find that the orientation-reversing nature of the shear

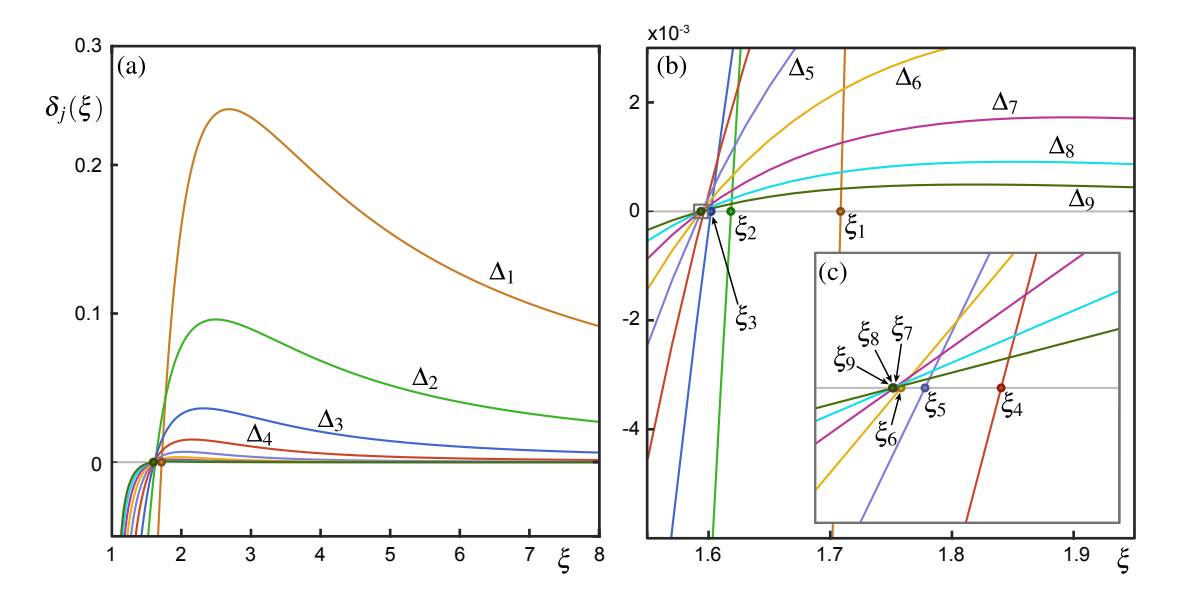


Figure 12: The signed difference functions $\delta_j(\xi)$ for $\alpha = 4.2$ and $\beta = -0.3$ of the gaps Δ_j for $j = 1, \ldots, 9$ with $\xi > 1$. Panel (a) shows them for $\xi \in (1, 8]$, and panels (b) and (c) are successive enlargements near the zeros ξ_j ; compare with Figure 9.

has serious implications for what the relevant gaps Δ_j are and how they are bounded in the projection onto the \bar{z} -axis. For $\xi \ll -1$ they are, indeed, still given by the respective accessible boundary of the horseshoe of h, as in the (unchanged) projection onto the \bar{y} -axis. However, as ξ is increased towards -1, the boundaries near where the gaps Δ_j close are now formed by the stable manifold $W^s(p_2)$ of the period-two point $p_2 = \{p_2^1, p_2^2\}$ from (11). In other words, the geometric mechanisms for the creation of blenders cannot be understood by the manifolds of fixed points alone, as was the case for orientation-preserving shear in Section 3.

Figure 13 shows four phase portraits of \mathcal{H} in the cylinder \mathcal{C} in the style of Figure 4; here, the first column is for $\beta = 0.3$ and the second column for $\beta = -0.3$, with $\xi = -1.8$ for the top row and $\xi = -1.5$ for the bottom and row. Shown are the fixed points p^{\pm} , the period-two orbit $p_2 = \{p_2^1, p_2^2\}$, and their one-dimensional stable manifolds $W^s(p^{\pm})$ and $W^s(p_2)$, computed up to 2^{10} intersection points of each manifold with the shown section Σ . For the case of an orientation-reversing shear, we now define this section as

$$\Sigma := \{ (\bar{x}, \bar{y}, \bar{z}) \in \mathcal{C} \mid \bar{x} = 0 \text{ and } \bar{y} > 0 \}.$$

This choice of Σ provides a wide spacing of intersection points; it lies on the other side of \mathcal{C} and is 'the other half' of the section we used for an orientation-preserving shear in Section 3; note that the viewpoint of Figure 13 has been rotated compared to Figures 4 and 5(a).

The three manifolds $W^s(p^-)$, $W^s(p^+)$ and $W^s(p_2)$ shown in Figure 13 are completely intermingled and cannot be distinguished. In the first row they are spread over a range of \bar{z} -values, with clear gaps in side projections; this is evidence that Λ is not a blender for $\xi = -1.8$. Notice the different structure of the visible gaps in panels (a1) and (b1): in the order of increasing width, they lie on either side of a central curve. This is a significant difference with the case of an orientation-preserving shear in Figure 4(a1) and (b1). The highlighted curve in Figure 13 is the very first segment of $W^s(p^+)$ near p^+ , and its role for the organisation of the gaps is discussed in Section 4.1.2. In the second row, on the other hand, there are no visible gaps when these manifolds are seen from the side, which suggests that for $\xi = -1.5$ the hyperbolic set Λ is a blender. For either column, the top-down views of the panels in Figure 13, or more precisely, their projections onto the Poincaré disk \mathcal{D} , are still the oriented and nonoriented horseshoes

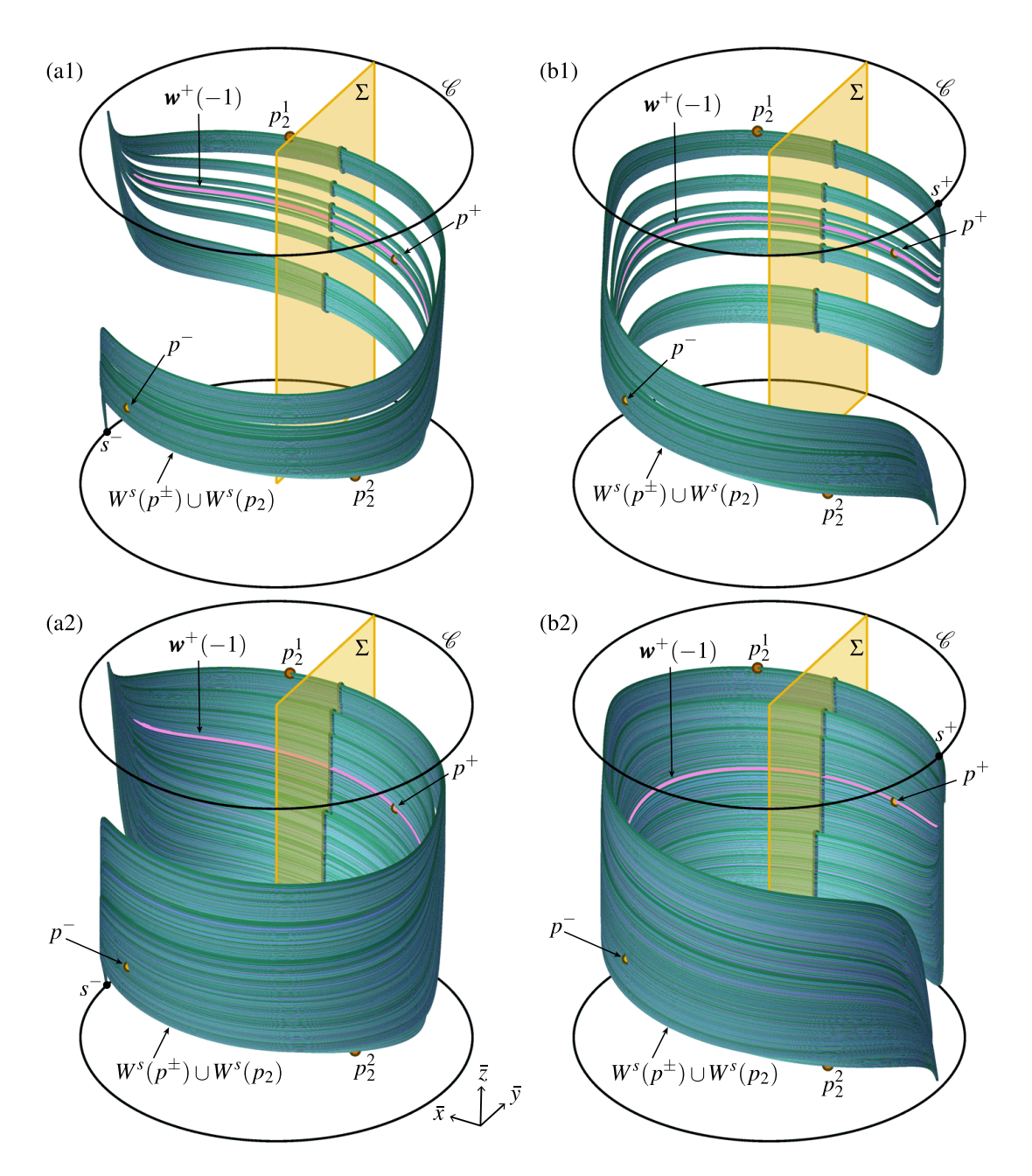


Figure 13: Phase portrait of \mathcal{H} in \mathcal{C} for $\xi < -1$. Panels (a1) and (a2) are for $\beta = 0.3$ with $\xi = -1.8$ and $\xi = -1.5$, and panels (b1) and (b2) for $\beta = -0.3$ with $\xi = -1.8$ and $\xi = -1.5$, respectively. Shown are p^{\pm} (golden dots), the period-two orbit $p_2 = \{p_2^1, p_2^2\}$ (red dots), their stable manifolds $W^s(p^-)$ (blue), $W^s(p^+)$ (purple) and $W^s(p_2) = W^s(p_2^1) \cup W^s(p_2^2)$ (dark and light green), and Λ (black dots). Also shown are Σ (sand colour), the central curve (pink) of $W^s(p^+)$ near p^+ , and the points q^{\pm} and s^+ or s^- (black dots) on $\partial \mathcal{C}$.

from panels (a2) and (b2) of Figure 3, respectively.

For the case of an orientation-reversing shear, it turns out that we need to study the stable manifold $W^s(p_2)$ of the period-two orbit $p_2 = \{p_2^1, p_2^2\}$. It consists of the two submanifolds $W^s(p_2^1)$ and $W^s(p_2^2)$, which are orientation-reversing; their two branches are computed as the stable manifolds of the fixed points p_2^1 and p_2^2 under \mathcal{H}^{-4} . Under \mathcal{H}^{-1} , these four branches cycle

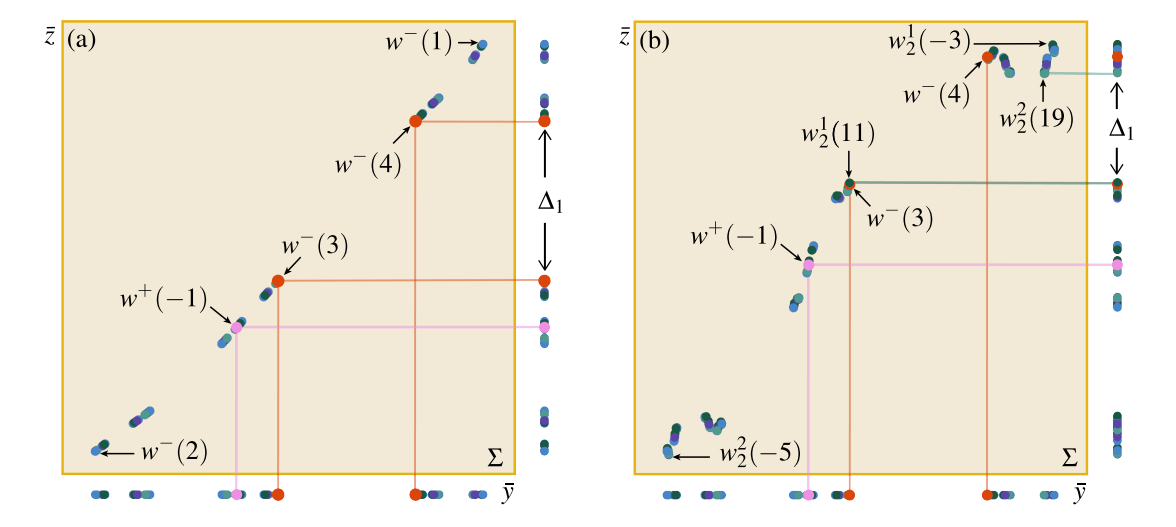


Figure 14: Intersection sets $\{w^-(l)\}$ (blue dots), $\{w^+(l)\}$ (purple dots), $\{w^2_1(l)\}$ (dark green dots) and $\{w^2_2(l)\}$ (light green dots) in Σ and in projection onto the \bar{z} - and \bar{y} -axes, for $\xi = -6.0$ (a) and $\xi = -2.5$ (b). There are 2^{10} points in each intersection set; labelled are the outermost intersection points and those bounding the main gap Δ_1 in projection onto the \bar{z} -axes, while $w^-(3)$ and $w^-(4)$ are highlighted in red, and $w^+(-1)$ is highlighted in pink. Here, $\alpha = 4.2$ and $\beta = 0.3$; compare with Figures 6.

as follows:

$$W_{+}^{s}(p_{2}^{1}) \to W_{+}^{s}(p_{2}^{2}) \to W_{-}^{s}(p_{2}^{1}) \to W_{-}^{s}(p_{2}^{2}) \to W_{+}^{s}(p_{2}^{1}),$$
 (19)

where W^s_{\pm} refers to the respective branch that initially extends to positive and negative \bar{x} -values, respectively. This information is useful for understanding the organisation of the corresponding intersection points with the section Σ , which we define as in Section 3. Namely, for a fixed value of ξ , we denote by $w^1_2(l) = w^1_2(l;\xi)$ and $w^2_2(l) = w^2_2(l;\xi)$ the l^{th} intersection point of the curves $W^s(p^1_2)$ and $W^s(p^2_2)$ with Σ , respectively, where the sign of $l \in \mathbb{Z} \setminus \{0\}$ distinguishes the respective two branches W^s_{\pm} as defined above. Moreover, we define and study the ξ -parametrised curves

$$\boldsymbol{w}_{2}^{1,2}(l) := \left\{ w_{2}^{1,2}(l;\xi) \mid \xi \in [\xi_{a}, \xi_{b}] \right\} \subset \Sigma \times [\xi_{a}, \xi_{b}]$$

over a ξ -range $[\xi_a, \xi_b]$ of interest, where l is selected from a suitable index set $\mathcal{L} \subset \mathbb{Z} \setminus \{0\}$. As is the case for $\boldsymbol{w}^{\pm}(l)$, the curves $\boldsymbol{w}_2^1(l)$ and $\boldsymbol{w}_2^2(l)$ can be computed accurately with the improved algorithm from [15].

4.1 Oriented horseshoe with $\xi < -1$

Our investigation of the nonorientable map \mathcal{H} with $\xi < -1$ and an oriented horseshoe for $\beta = 0.3$ starts with the consideration of the intersection set $W^s(\Lambda) \cap \Sigma$ for one ξ -value sufficiently far from and one closer to -1. For this purpose, Figure 14 shows 2^{10} points each of the intersection sets $\{w^{\pm}(l)\}$, $\{w_2^1(l)\}$ and $\{w_2^2(l)\}$ in Σ with their projections onto the \bar{y} - and \bar{z} -axes. For $\xi = -6.0$ in panel (a), these two projections are topologically the same and all intersection points seems to lie on the graph of a now monotonically increasing function (this change of 'direction' is due to the different choice of section). In particular, the main gap labelled Δ_1 is again bounded by the points $w^-(3)$ and $w^-(4)$ for both projections; compare with Figure 6(a1). For the larger value of $\xi = -2.5$ in Figure 14 (b), this is no longer the case. Nested U-shaped clusters of intersection points have developed. More importantly, we find the new feature that the main gap Δ_1 is

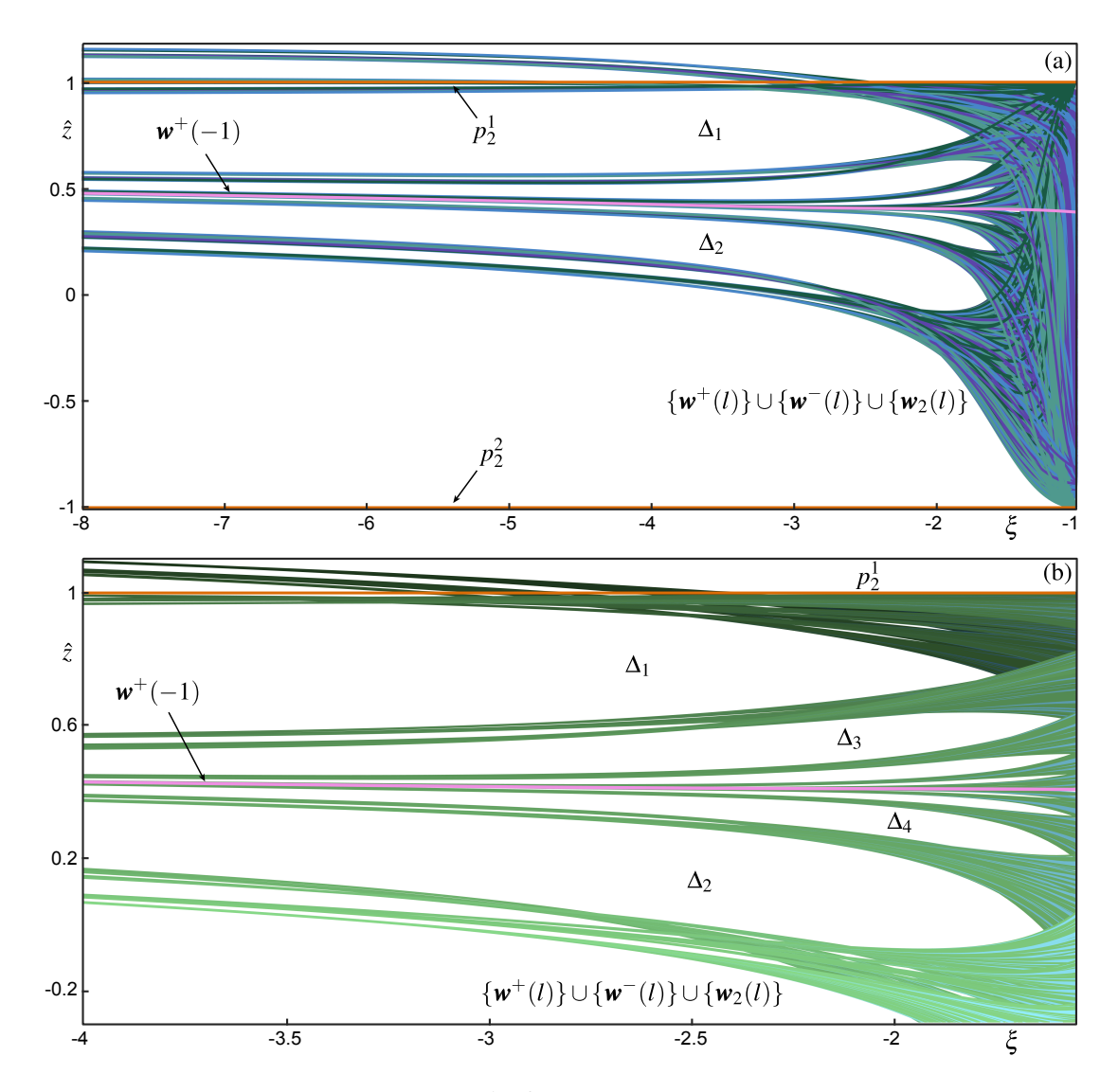


Figure 15: The period-two orbit $p_2 = \{p_2^1, p_2^2\}$ (orange curves) and the sets $\{\boldsymbol{w}^+(l)\}$, $\{\boldsymbol{w}^-(l)\}$ and $\{\boldsymbol{w}_2(l)\} = \{\boldsymbol{w}_2^1(l)\} \cup \{\boldsymbol{w}_2^2(l)\}$ with 2^{10} computed curves each, shown in the rescaled (ξ, \hat{z}) -plane, where $p_2^1 = 1$ and $p_2^2 = -1$. Panel (a) shows the range $\xi \in [-8, -1.02]$ with $\{\boldsymbol{w}^-(l)\}$ in blue, $\{\boldsymbol{w}^+(l)\}$ in purple, $\{\boldsymbol{w}_2^1(l)\}$ in dark green, and $\{\boldsymbol{w}_2^2(l)\}$ in light green; panel (b) shows an enlargement, where the curves in $\{\boldsymbol{w}^\pm(l)\}$ are coloured in a dark to light cyan gradient, and $\{\boldsymbol{w}_2(l)\}$ in a dark to light green gradient, both based on the value of their \bar{y} -coordinate. The central curve $\boldsymbol{w}^+(-1)$ is highlighted in pink, and the largest gaps are labelled. Here, $\alpha = 4.2$ and $\beta = 0.3$; compare with Figure 7.

bounded by a point in $\{w_2^1(l)\}$ at the bottom and a point in $\{w_2^2(l)\}$ at the top; likewise, the points at the very top and bottom on the \bar{z} -axis are also from these intersections sets of the period-two orbit p_2 .

4.1.1 The carpet of carpets for $\beta > 0$ with $\xi < -1$

We investigate this observation further by presenting in Figure 15 the carpet of carpets consisting of the corresponding ξ -parametrised intersection curves $\{\boldsymbol{w}^+(l)\}$, $\{\boldsymbol{w}^-(l)\}$ and $\{\boldsymbol{w}_2(l)\} = \{\boldsymbol{w}_2^1(l)\} \cup \{\boldsymbol{w}_2^2(l)\}$. They were rendered from computed data with a uniform ξ -mesh of mesh size 0.02 and are shown in the rescaled (ξ, \hat{z}) -plane, with \hat{z} now defined such that the two period-two

points p_2^1 and p_2^2 lie at ± 1 . The central curve $\boldsymbol{w}^+(-1)$ is highlighted, and the gaps Δ_1 up to Δ_4 are labelled. Panel (a) shows the ξ -range [-8.0, -1.02], where the four sets of intersection curves are distinguished by colour. For sufficiently small negative ξ , the curves are ordered on the \hat{z} -axis as given by the Cantor set of the stable manifolds of the oriented horseshoe, as was shown in Figure 14(a). However, as ξ increases, the curves start to intersect and a recognisable sequence of largest gaps Δ_j emerges; these gaps then close in succession when ξ is increased further, indicating that the hyperbolic set Λ is a blender near $\xi = -1$. The process of crossing intersection curves is illustrated differently in the enlarged view of Figure 15(b), where the curves in $\{\boldsymbol{w}^{\pm}(l)\}$ and $\{\boldsymbol{w}_2(l)\}$ are shown in shades of cyan and green, respectively, as determined by their \bar{y} -values; compare with Figure 7(b).

Figure 15 shows that the general scenario of successively closing gaps is also found for an orientation-reversing shear. However, there is an important difference: the gaps Δ_j are now found on both sides of the highlighted curve $\boldsymbol{w}^+(-1)$. This curve corresponds to the point $\boldsymbol{w}^+(-1)$ in Figure 14, and it plays the role of a 'symmetry axis' in the (ξ,\hat{z}) -plane onto which the Δ_j accumulate on both sides. Note in Figure 15 that, owing to the orientation-reversing nature of \mathcal{H} in the z-directions, the situation above $\boldsymbol{w}^+(-1)$ for Δ_j with odd j=2k+1 is topologically as that below $\boldsymbol{w}^+(-1)$ for Δ_j with even j=2k. The relevant gaps Δ_j are again defined by specific gaps of the Cantor structure of $W^s(\Lambda_h)$. As before, Δ_1 is the first gap at level 1 with \hat{y} -values around 0, but now Δ_j is alternatingly the left and the right gap (of lower and higher \hat{y} -value, respectively) at each level; compare with Figure 14. Note that this characterisation of the Δ_j for $\xi < -1$ is compatible with that for $\xi > 1$: the second iterate \mathcal{H}^2 preserves orientation in the z-directions and its relevant gaps are Δ_{2j+1} and Δ_{2j} , respectively; each of these subsequences converges to $\{\boldsymbol{w}^+(-1)\}$ from the corresponding side.

4.1.2 The boundary curves of the relevant gaps for $\beta > 0$ with $\xi < -1$

Figure 15 shows that there are again well-defined intersection curves that bound the different gaps as ξ is increased. Its panel (a) presents the specific curves that bound the first six gaps Δ_j for $\xi \ll -1$ and near their crossing points c_j , and panel (b) is an enlargement near where these gaps close. While this is still clearly a carpet of carpets, there are differences compared to the case $\xi \gg 1$. First of all, due to the 'reflection' with respect to the central curve $\boldsymbol{w}^+(-1)$, the bottom boundary of Δ_j with odd j, which is nearer $\boldsymbol{w}^+(-1)$, corresponds to the top boundary for even j, which is again nearer to $\boldsymbol{w}^+(-1)$; we refer to this sequence as the near boundaries and indicate objects on them with a superscript -. The far boundaries are defined in complete analogy and objects on them are indicated with a superscript +. Secondly, the second difference with the orientable case is that both the near and far boundaries feature ξ -ranges of many crossings of curves, with begin points b_j^{\pm} and end points e_j^{\pm} ; this is illustrated by the two insets of Figure 15(a).

Finally, in contrast to the case of positive ξ , the boundaries of the gaps Δ_j near where they close are now formed by the intersection points $\{\boldsymbol{w}_2(l)\} = \{\boldsymbol{w}_2^1(l)\} \cup \{\boldsymbol{w}_2^2(l)\}$ of the stable manifold $W^s(p_2)$ of the period-two orbit p_2 . Note in Figure 15(b) that the points e_j^- and e_j^+ always lie to the left of the crossing point c_j ; Table 8 in the Appendix lists their ξ -values and the respective second intersection curves defining them, which are also from $\{\boldsymbol{w}_2(l)\}$. The left block of Table 4 lists the specific pairs of near and far boundary curves in $\{\boldsymbol{w}_2(l)\}$ that bound the gaps Δ_j near c_j for $1 \leq j \leq 8$, as determined by our computation of $W^s(p_2)$; note that they each follow the mapping rule (19). This data allows us to derive recurrence relations for the near and far boundaries of the gaps Δ_j near c_j as follows. For the near boundaries $\boldsymbol{w}_2^2(a_j^-)$ for even j > 1 and $\boldsymbol{w}_2^1(a_j^-)$ for odd $j \geq 1$, we have

$$a_{j+1}^- = 2[(-1)^{j+1}a_j^- - \mathbf{1}_4(j+1)] + 1$$
 with $a_1 = -1$,

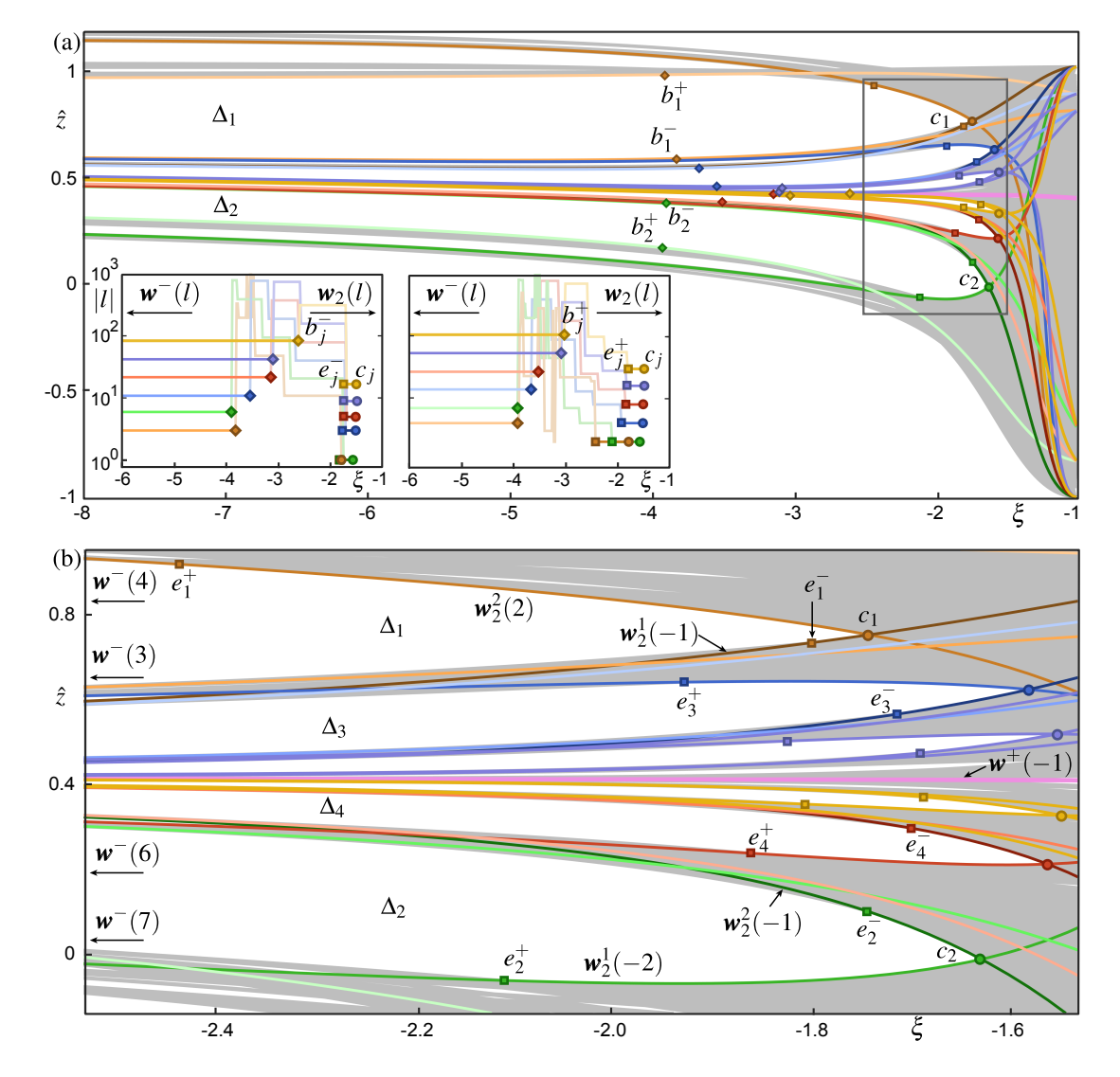


Figure 16: Boundary curves of the gaps Δ_1 to Δ_6 in the (ξ, \hat{z}) -plane for $\alpha = 4.2$ and $\beta = 0.3$, overlaid in colour onto $\{\boldsymbol{w}^{\pm}(l)\}$ and $\{\boldsymbol{w}_2(l)\} = \{\boldsymbol{w}_2^1(l)\} \cup \{\boldsymbol{w}_2^2(l)\}$ (grey) from Figure 15(a). Also labelled are the closing points c_j , and the begin and end points b_j^{\pm} and e_j^{\pm} that bound the ξ -range of crossing curves; the central curve $\boldsymbol{w}^+(-1)$ is highlighted in pink. Panel (a) is over the range $\xi \in (-8, -1]$, and its inset shows the corresponding modulus of the indices |l| versus ξ for the (alternating) bottom and top boundaries of Δ_j , respectively. Panel (b) is an enlargement of the frame in panel (a) around where the gaps Δ_j close.

and for the far boundaries $\boldsymbol{w}_2^1(a_j^+)$ for even j>1 and $\boldsymbol{w}_2^2(a_j^+)$ for odd $j\geq 1$, we have

$$a_{j+1}^+ = 2[(-1)^j a_j^+ - \mathbf{1}_4(j+3)]$$
 with $a_1 = 2$.

Recall from (18) that the indicator function $\mathbf{1}_4(n)$ is 0, except when n is a multiple of 4. The respective indices defining the near and far boundaries of the gaps Δ_j near c_j are readily computed with these recurrences, but we found that solving them in explicit form does not lead to practical expressions.

Rather, we are able to shed further light on the nature of these boundaries by considering p_2^1 and p_2^2 as fixed points of the second iterate \mathcal{H}^2 and realising that $W^s(p_2^1)$ and $W^s(p_2^1)$ are both nonoriented under \mathcal{H}^2 . We find that the odd and even subsequences of (a_j^-) and (a_j^+) are not Lucas sequences (again, because of an additional alternating term). In the same spirit as

Closing of gaps Δ_j for $\xi < -1$ and $\beta = 0.3$

| | boundin | bounding curves | | ξ -value of c_j | | | | |
|----------|----------------------|----------------------------|--|-----------------------|---------------|---------|--|--|
| j | $e_j^- < \xi < c_j$ | $e_j^+ < \xi < c_j$ | | ξ_j | d_{j} | r_{j} | | |
| 1 | $w_2^1(-1)$ | $w_2^2(2)$ | | -1.740071 | | | | |
| 2 | $w_2^{\bar{2}}(-1)$ | $ w_2^{\bar{1}}(-2) $ | | -1.627098 | 0.112973 | | | |
| 3 | $w_2^{\bar{1}}(3)$ | $ w_2^{\overline{2}}(-4) $ | | -1.579257 | | | | |
| 4 | $w_2^2(5)$ | $ w_2^1(8) $ | | -1.558866 | 0.020392 | 0.4262 | | |
| 5 | $w_2^{\bar{1}}(-9)$ | $ w_2^{\bar{2}}(16) $ | | -1.550285 | 0.008580 | 0.4207 | | |
| 6 | $w_2^{\bar{2}}(-17)$ | $ w_2^{\bar{1}}(-30) $ | | -1.546641 | 0.003644 | 0.4246 | | |
| 7 | $w_2^{\bar{1}}(35)$ | $ w_2^{\bar{2}}(-60) $ | | -1.543628 | 0.002443 | | | |
| 8 | $w_2^{\bar{2}}(69)$ | $ w_2^{\bar{1}}(120) $ | | -1.542356 | 0.001272 | | | |
| ∞ | | | | -1.541979 | $pprox \xi^*$ | | | |

Table 4: Curves from $\{\boldsymbol{w}^{-}(l)\}$ and $\{\boldsymbol{w}^{+}(l)\}$ that form the boundaries of Δ_{j} near the closing points c_{j} for $\xi < -1$ and $\beta = 0.3$ (left block), and computed ξ_{j} -values of c_{j} with consecutive differences $d_{j} = |\xi_{j} - \xi_{j-1}|$ and contraction rates $r_{j} = d_{j}/d_{j-1}$ (right block); also shown is the resulting limit ξ^{*} .

in Section 3.2, this motivates us to consider the fourth iterate \mathcal{H}^4 , which maps each branch of these two manifolds to itself. We obtain the following quartary recursion relations: for the near boundary

$$a_{j+4}^{-} = 16a_{j}^{-} + \begin{cases} 7, & \text{if 4 divides } (j+3), \\ -1, & \text{if 4 divides } (j+2), \\ -13, & \text{if 4 divides } (j+1), \\ -11, & \text{if 4 divides } j, \end{cases}$$

and for the far boundary

$$a_{j+4}^- = 16a_j^- + \begin{cases} -16, & \text{if 4 divides } (j+3), \\ 2, & \text{if 4 divides } (j+2), \\ 4, & \text{if 4 divides } (j+1), \\ -8, & \text{if 4 divides } j. \end{cases}$$

All of these four subsequences of both (a_j^-) and (a_j^+) are Lucas sequences that satisfy the same recursion

$$R_k = 17R_{k-1} - 16R_{k-2}, (20)$$

with the respective first two indices modulo 4 from Table 4 as the seeds R_1 and R_2 .

4.1.3 The limit of the closing points c_i for $\beta > 0$ with $\xi < -1$

Having identified the bounding curves near the closing points c_j , we show in Figure 17 the graphs of the difference functions $\delta_j(\xi)$ of the gaps Δ_j for $1 \leq j \leq 8$ near their respective zeros ξ_j . As is the case when $\xi > 1$, we again find that the gaps Δ_j close one after the other, now as ξ is increased, that is $\xi_j < \xi_{j+1}$. The convergence of the values ξ_j is also fast in this case, and we determine their values again by local cubic spline interpolation through data on a finer mesh of size 0.004 over the relevant range. The right block of Table 4 shows the resulting values of ξ_j for $1 \leq j \leq 8$, with their consecutive differences d_j and contraction rates r_j (only shown up to j = 6 due to loss of significant digits). Note the considerably larger limiting contraction rate of about 0.42, compared to those of about 0.29 and 0.32 in Section 3, and observe that Δ_8 and its bounding curves already lie extremely close to the central curve $w^+(-1)$ so that

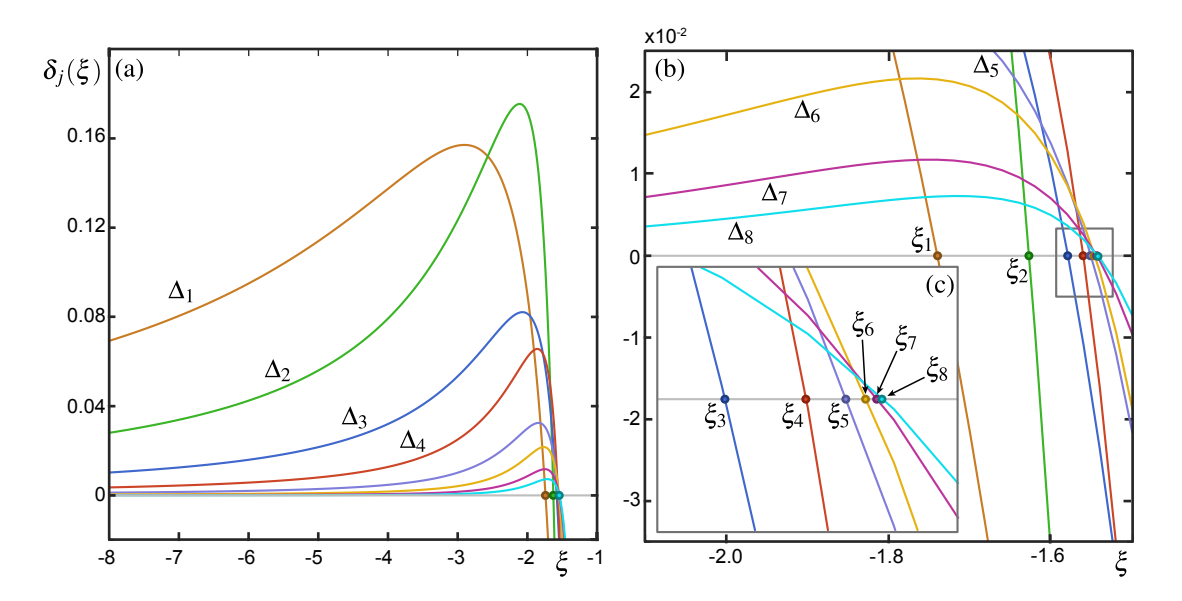


Figure 17: The signed difference functions $\delta_j(\xi)$ for $\alpha = 4.2$ and $\beta = 0.3$ of the gaps Δ_j for $j = 1, \ldots, 8$ with $\xi < -1$. Panel (a) shows them for $\xi \in (-8, -1]$, and panels (b) and (c) are successive enlargements near the zeros ξ_j ; compare with Figure 9.

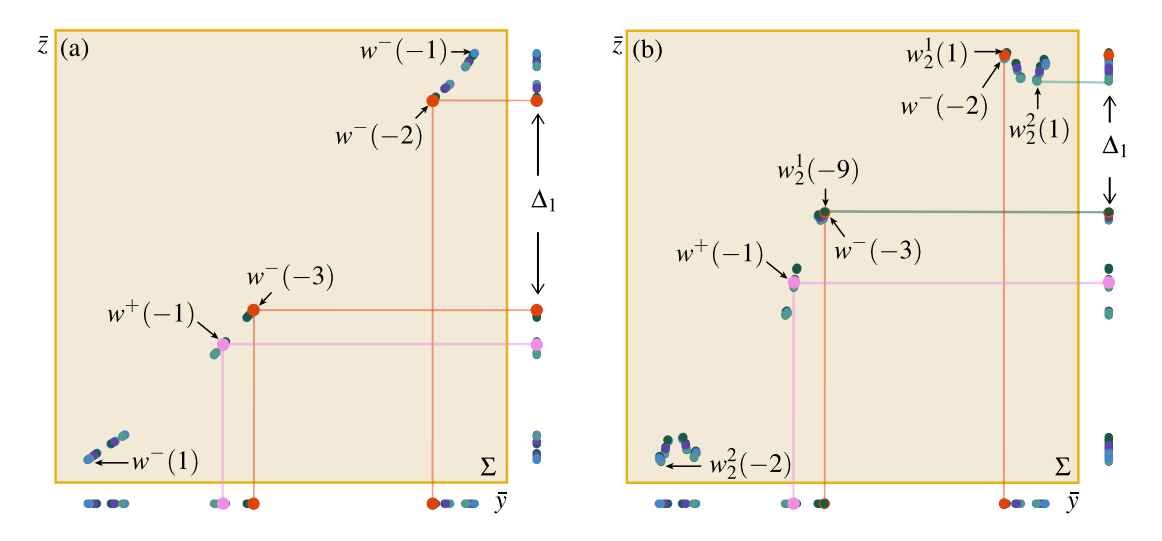


Figure 18: Intersection sets $\{w^-(l)\}$ (blue dots), $\{w^+(l)\}$ (purple dots), $\{w_1^2(l)\}$ (dark green dots) and $\{w_2^2(l)\}$ (light green dots) in Σ and in projection onto the \bar{z} - and \bar{y} -axes, for $\xi = -6.0$ (a) and $\xi = -2.5$ (b). There are 2^{10} points in each intersection set; labelled are the outermost intersection points and those bounding the main gap Δ_1 in projection onto the \bar{z} -axes, while $w^-(-1)$ and $w^-(-1)$ are highlighted in red, and $w^+(-1)$ is highlighted in pink. Here, $\alpha = 4.2$ and $\beta = -0.3$; compare with Figures 10 and 14.

they cannot be distinguished in Figure 16. This is why we are able to present reliable values of ξ_j only up to j=8 in Table 4. Nevertheless, their values clearly stabilise and we obtain the estimate $\xi^* \approx -1.541979$ for the limit. Hence, we conclude from this numerical evidence that Λ is a blender for any $\xi^* < \xi < -1$.

Closing of gaps Δ_i for $\xi < -1$ and $\beta = -0.3$

| | boundin | bounding curves | | ξ -value of c_j | | | | |
|----------|-----------------------------|-----------------------|--|-----------------------|---------------|---------|--|--|
| j | $e_j^- < \xi < c_j$ | $e_j^+ < \xi < c_j$ | | ξ_j | d_{j} | r_{j} | | |
| 1 | $w_2^1(-1)$ | $w_2^2(1)$ | | -1.687353 | | | | |
| 2 | $w_2^{\bar{2}}(3)$ | $w_2^{\bar{1}}(3)$ | | -1.614872 | 0.072480 | | | |
| 3 | $oldsymbol{w}_2^{ar{1}}(7)$ | $w_2^{\bar{2}}(-5)$ | | -1.596029 | 0.018843 | 0.2599 | | |
| 4 | $w_2^{\bar{2}}(-13)$ | $w_2^{\bar{1}}(-9)$ | | -1.587668 | 0.008361 | 0.4437 | | |
| 5 | $w_2^{\bar{1}}(-25)$ | $w_2^{\bar{2}}(19)$ | | -1.584156 | 0.003512 | 0.4200 | | |
| 6 | $w_2^{\bar{2}}(51)$ | $w_2^{\bar{1}}(39)$ | | -1.582677 | 0.001479 | 0.4210 | | |
| 7 | $w_2^{\bar{1}}(103)$ | $w_2^{\bar{2}}(-77)$ | | -1.582006 | 0.000671 | | | |
| 8 | $m{w}_2^{ar{2}}(-205)$ | $w_2^{\bar{1}}(-153)$ | | -1.581708 | 0.000297 | | | |
| ∞ | | | | -1.581620 | $pprox \xi^*$ | | | |

Table 5: Curves from $\{w^-(l)\}$ and $\{w^+(l)\}$ that form the boundaries of Δ_j near the closing points c_j for $\xi < -1$ and $\beta = -0.3$ (left block), and computed ξ_j -values of c_j with consecutive differences $d_j = |\xi_j - \xi_{j-1}|$ and contraction rates $r_j = d_j/d_{j-1}$ (right block); also shown is the resulting limit ξ^* .

4.2 Nonoriented horseshoe with $\xi < -1$

When h is orientation reversing and has the nonoriented full horseshoe shown in Figure 3(b), the map \mathcal{H} is orientation preserving due to the orientation-reversing shear. Figure 18 for $\beta = -0.3$ shows the intersection sets $W^s(p^\pm) \cap \Sigma$ and $W^s(p_2) \cap \Sigma$, for $\xi = -6.0$ in panel (a) and $\xi = -2.5$ in panel (b). For $\xi = -6.0$, these intersection sets reveal the same structure we found for the case of positive ξ in Section 3.2: all points lie on a the graph of a monotonically increasing function, so that its two projections onto the \bar{y} - and the \bar{z} -axis are homeomorphic; in particular, the gaps of this Cantor set are bounded in both projections by points in $W^s(p^\pm) \cap \Sigma$. For $\xi = -2.5$ in Figure 18(b), this is no longer the case and gaps in projection onto the \bar{z} -axis are now bounded by points in $W^s(p_2) \cap \Sigma$. This is similar to what we found in Section 4.1, but the boundaries of the gaps are given by different points of $\{w_1^2(l)\}$ and $\{w_2^2(l)\}$, respectively; compare with Figure 14(b).

Figure 19 shows the corresponding curves in $\{\boldsymbol{w}^{\pm}(l)\}$, $\{\boldsymbol{w}_{1}^{2}(l)\}$ and $\{\boldsymbol{w}_{2}^{2}(l)\}$, where the central curve $\boldsymbol{w}^{+}(-1)$ is again highlighted. Due to the orientation-reversing nature of the shear, the gaps Δ_{j} lie again alternatingly on either side of the central curve, as in Figure 16; moreover, we also find in Figure 19 begin points b_{j}^{\pm} and end points e_{j}^{\pm} of many crossings of curves that bound the near and far boundaries of Δ_{j} . The points e_{j}^{\pm} are always to the left of the closing point c_{j} (see Table 8 in the Appendix), so that the boundary of Δ_{j} near c_{j} is formed by specific curves in $\{\boldsymbol{w}_{2}(l)\} = \{\boldsymbol{w}_{2}^{1}(l)\} \cup \{\boldsymbol{w}_{2}^{2}(l)\}$. These were identified for $1 \leq j \leq 8$ and are listed in the left block of Table 4, allowing us to derive the following recurrence relations. For the near boundaries $\boldsymbol{w}_{2}^{2}(a_{j}^{-})$ for even j > 1 and $\boldsymbol{w}_{2}^{1}(a_{j}^{-})$ for odd $j \geq 1$, we find

$$a_{j+1}^- = 2(-1)^j a_j^- + 1$$
 with $a_1 = -1$,

and for the far boundaries $\boldsymbol{w}_{2}^{1}(a_{i}^{+})$ for even j>1 and $\boldsymbol{w}_{2}^{2}(a_{i}^{+})$ for odd $j\geq1$, we find

$$a_{j+1}^+ = -2(-1)^j a_j^+ + 1$$
 with $a_1 = 1$.

The secondary recurrence relations for \mathcal{H}^2 are given by

$$a_{j+2}^b = -4a_j^b + \begin{cases} 3 & \text{if } j \text{ is odd,} \\ -1 & \text{if } j \text{ is even,} \end{cases}$$

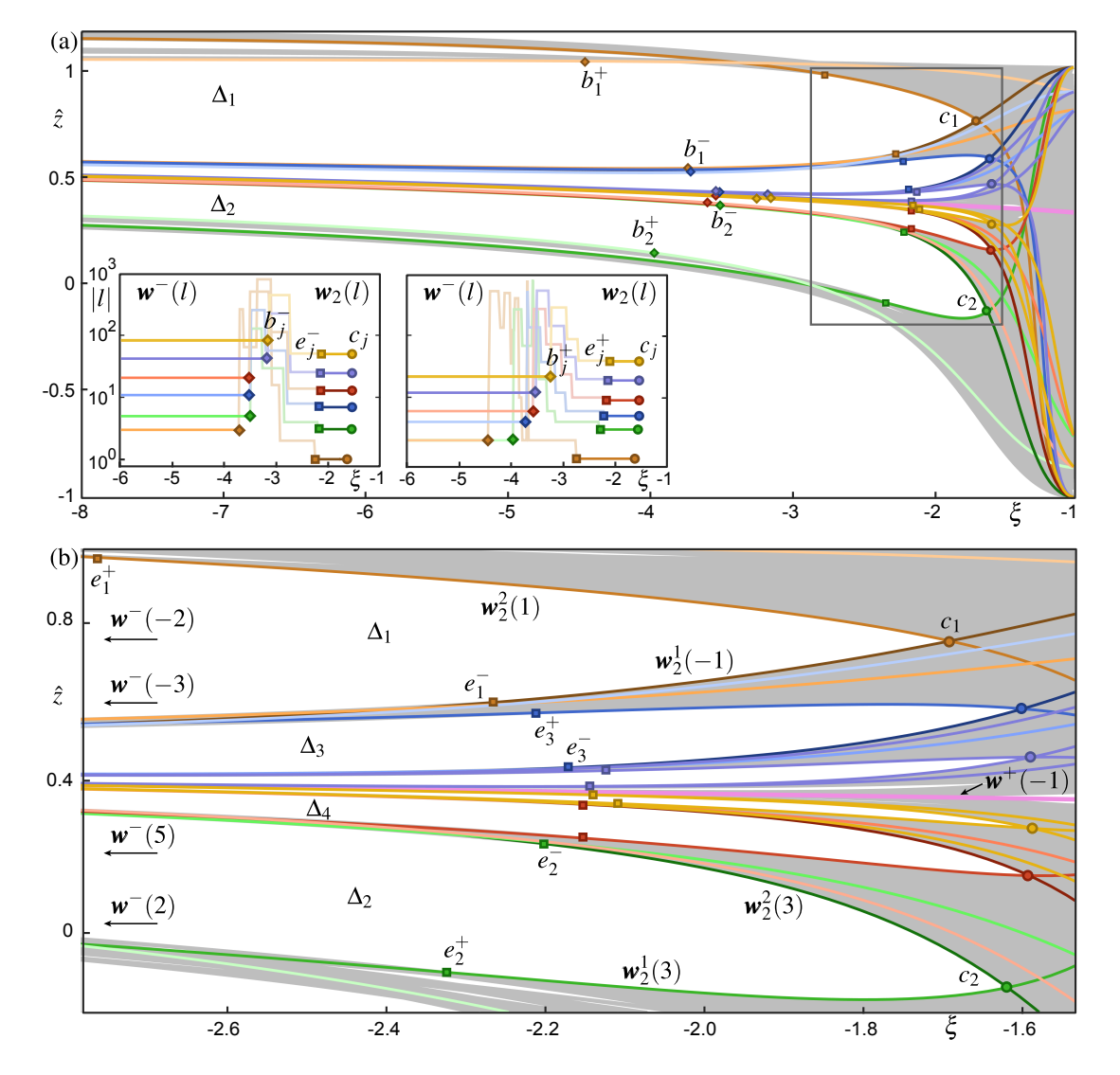


Figure 19: Boundary curves of the gaps Δ_1 to Δ_6 in the (ξ, \hat{z}) -plane for $\alpha = 4.2$ and $\beta = -0.3$, overlaid in colour onto $\{\boldsymbol{w}^{\pm}(l)\}$ and $\{\boldsymbol{w}_2(l)\} = \{\boldsymbol{w}_2^1(l)\} \cup \{\boldsymbol{w}_2^2(l)\}$ (grey). Also labelled are the closing points c_j , and the begin and end points b_j^{\pm} and e_j^{\pm} that bound the ξ -range of crossing curves; the central curve $\boldsymbol{w}^+(-1)$ is highlighted in pink. Panel (a) is over the range $\xi \in (-8, -1]$, and its inset shows the corresponding modulus of the indices |l| versus ξ for the (alternating) far and near boundaries of Δ_j , respectively. Panel (b) is an enlargement of the frame in panel (a) around where the gaps Δ_j close. Compare with Figure 16.

for the near boundary, and

$$a_{j+2}^t = 4a_j^t + \begin{cases} 2 & \text{if } j \text{ is odd,} \\ 1 & \text{if } j \text{ is even.} \end{cases}$$

for the far boundary. All of these odd and even subsequences are Lucas sequences that satisfy the recurrence

$$R_k = -3R_{k-1} + 4R_{k-2},$$

with the respective first two odd and even indices from Table 4 as R_1 and R_2 . Moreover, consider the action of \mathcal{H}^4 , which maps each branch of $W^s(p_2^1)$ and of $W^s(p_2^1)$ to itself, we find that the four subsequences of every fourth point of both (a_j^-) and (a_j^+) also satisfy the recurrence (20) from Section 4.1.2, with the corresponding seeds R_1 and R_2 from Table 5.

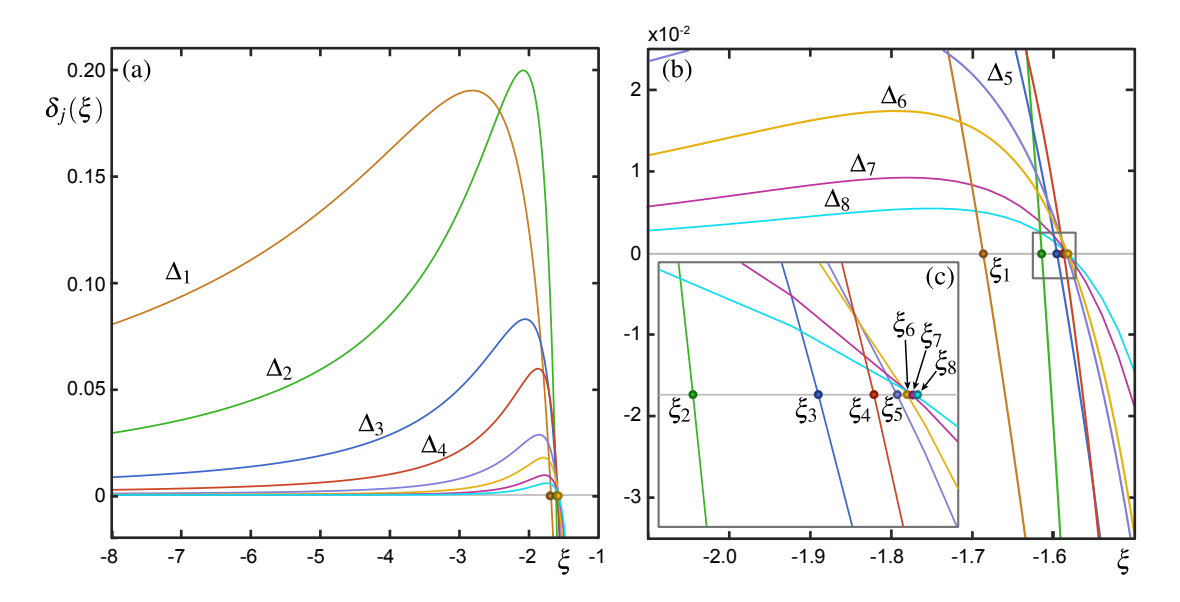


Figure 20: The signed difference functions $\delta_j(\xi)$ for $\alpha = 4.2$ and $\beta = -0.3$ of the gaps Δ_j for j = 1, ..., 8 with $\xi < -1$. Panel (a) shows them for $\xi \in (-8, -1]$, and panels (b) and (c) are successive enlargements near the zeros ξ_j ; compare with Figure 17.

The knowledge of the specific boundary curves of Δ_j near c_j gives the signed difference functions $\delta_j(\xi)$ that are shown in Figure 20 for $1 \leq j \leq 8$. The closing values ξ_j of its zeros were again determined by spline interpolation from a mesh of size 0.004; as before, they are again ordered and converge fast. Precise values are listed in the right block of Table 5 with the corresponding values of differences d_j and contraction rates r_j (again, only up to j = 6). This data gives the estimate $\xi^* \approx -1.581602$ for the limit, and we conclude that $W^s(\Lambda)$ has the carpet property and Λ is a blender for ξ above this value and up to $\xi = -1$.

5 Conclusions

We investigated how blenders may emerge in the explicitly given three-dimensional Hénon-like family \mathcal{H} as parameters vary. Throughout, we fixed the classical Hénon parameters α and β so that the underlying two-dimensional Hénon map h has a full horseshoe in the (x,y)-plane. The corresponding transitive hyperbolic set Λ_h of h 'lifts' to the hyperbolic set Λ of \mathcal{H} due to the dynamics in the third coordinate z, which is a shear of strength ξ . When $|\xi|$ is very large, Λ is not a blender, while it is a blender when $|\xi|$ is sufficiently close to 1. We addressed the intertwined questions for which values of the shear parameter ξ the hyperbolic set Λ is a blender, and how the transition to a blender occurs as $|\xi|$ is decreased.

As a new aspect, we considered the two cases when the horseshoe of the two-dimensional diffeomorphism h is oriented or nonoriented, and further distinguished whether the shear is orientation-preserving or not. For all four cases of orientation, specified by signs of β and ξ , we presented the transition to a blender as $|\xi|$ approaches 1. To this end, we computed the one-dimensional stable manifolds of the relevant fixed and period-two points to very large arclength in the compactified $(\bar{x}, \bar{y}, \bar{z})$ -space. For each of these invariant manifolds, we indexed their successive intersection points with a chosen plane and considered them as a function of the parameter ξ . We determined how the resulting (many) smooth curves of intersection points with the same index l rearrange in the (ξ, \bar{z}) -plane and then become dense for $|\xi|$ sufficiently close to 1. This denseness in projection, also known as the carpet property, is a characterising property that allows one to determine the ξ -range of existence of a blender.

In contrast to earlier work, where the carpet property was verified by considering intersection points of manifolds as an unordered set, we determined the indices l of the specific curves of intersection points in the (ξ, \bar{z}) -plane that bound the relevant sequence of main gaps. Across the four possible orientations cases of \mathcal{H} , the organisation of the manifolds exhibits an overall consistent pattern. More specifically, we found that, from gap to gap, the indices satisfy two-stage recurrence relations that identify them as Lucas sequences. This topological information can be used to compute the precise ξ -values at which successive gaps close (in projection). The data we obtained in this way strongly suggests that these values form a geometric sequence. This allowed us to give accurate estimates for the respective limits ξ^* , which each constitutes a lower bound for the ξ -range over which the corresponding blender exists.

While there is an overall similarity, in both the ranges of ξ -values where \mathcal{H} has a blender and the mechanisms of how the carpet property emerges, differences exist between the four cases we considered. Namely, the bounding curves of intersection points in the (ξ, \bar{z}) -plane differ from case to case, and the respective indices satisfy different recurrence relations. Most importantly, for positive ξ , the boundaries of the gaps near where they close are formed by intersection points of the manifolds $W^s(p^+)$ and $W^s(p^-)$ of the fixed points p^{\pm} — while, for negative ξ , they are formed by the manifolds $W^s(p_2)$ and $W^s(p_2)$ of the period-two orbit $p_2 = \{p_2^1, p_2^1\}$, due the nonoriented nature of the shear.

Overall, we presented a detailed numerical and theoretical analysis of the mechanisms responsible for the creation of blenders in an explicit test-case example. This was achieved through the further development and refinement of the algorithm to compute one-dimensional manifolds of diffeomorphisms as arclength-parametrised curves. This enabled the computation of extremely long pieces of the relevant manifolds in compactified coordinates with high accuracy, even when they exhibit sharp turns. Consequently, we are able to find ordered intersection sets of the relevant manifolds with a plane and represent them as curves parametrised by ξ . This improved capability allowed us to observe and describe in unprecedented ways how their ordering in the relevant projection changes, and how gaps close and then the carpet property holds, showing the presence of a blender. More generally, our work demonstrates the effectiveness of advanced computational methods as a tool for obtaining insights into advanced concepts and for enriching the theoretical framework.

Our findings raise compelling questions regarding the generality of the transition leading to a blender and associated wild chaos. The pattern of the gaps and the geometric convergence of the ξ_j -values of the closing points support the idea that gaps close systematically and generically. Moreover, the Hénon map is not merely a theoretical construction, but it can actually be found in other dynamic systems. Specifically, systems exhibiting homoclinic tangencies can be considered a natural source for Hénon-like maps, as evidenced by various studies [20, 19, 51, 24, 23]. Thus, while our study focused on a constructed model exhibiting a blender, we anticipate that underlying mechanisms are universal and applicable to real-world systems.

An intriguing aspect of our research is the exact nature of the transition from a Cantor structure to a blender. When $|\xi|$ is sufficiently large, the expansion rate of the shear is much stronger than that of the Hénon map. Consequently, the dynamics is essentially confined to a two-dimensional repelling manifold and, thus, the Cantor structure of the two-dimensional Hénon map is seen in effectively any projection. Our calculations indicate a dramatic reorganisation of the one-dimensional stable manifolds as this property is lost for decreasing $|\xi|$. We conjecture that this transition is a continuous process and expect a similar transition to occur for other diffeomorphisms that may exhibit a blender. A related issue for further study is determining the source of the consistent contraction rates one observes in the closing of the gaps in projection. A first initial approach would be to investigate the eigenvalues of fixed and periodic points as potential indicators. However, a comprehensive understanding will require an in-depth examination of the expansion rates across the entire hyperbolic set Λ of \mathcal{H} .

Switching points s_i and end points e_i for $\xi > 1$ and $\beta = 0.3$

| | bottom | boundary |
|----------|------------------|-----------------------|
| j | $s_j < \xi$ | ξ -value of s_j |
| 1 | $ w^{-}(3) $ | 2.382781 |
| 2 | $ w^{-}(5) $ | 2.212111 |
| 3 | $ w^{-}(9) $ | 2.153697 |
| 4 | $ w^{-}(17) $ | 2.132794 |
| 5 | $ w^{-}(33) $ | 2.125143 |
| 6 | $ w^{-}(65) $ | 2.122285 |
| 7 | $ w^{-}(129) $ | 2.121205 |
| 8 | $ w^{-}(257) $ | 2.120797 |
| 9 | $ w^{-}(513) $ | 2.120643 |
| ∞ | | 2.120549 |

| top boundary | | | | | |
|-----------------|-----------------------|--|--|--|--|
| $e_j < \xi$ | ξ -value of e_j | | | | |
| $w^+(-2)$ | 2.141972 | | | | |
| $ w^{+}(4) $ | 2.087002 | | | | |
| $w^{+}(-6)$ | 2.067769 | | | | |
| $w^{+}(12)$ | 2.060911 | | | | |
| $w^+(-22)$ | 2.058417 | | | | |
| $w^{+}(44)$ | 2.057504 | | | | |
| $w^{+}(-86)$ | 2.057161 | | | | |
| $w^+(172)$ | 2.057034 | | | | |
| $ w^{+}(-342) $ | 2.056986 | | | | |
| • | 2.056956 | | | | |

Table 6: Switching point and end point data for $\xi > 1$ and $\beta = 0.3$; see Section 3.1.

We finish by mentioning two related directions of ongoing research. First of all, it will be interesting to investigate, in the same spirit, the occurence of heterodimensional cycles, which are a means to show the robust occurence of structurally unstable dyanamics. The only example of an explicitly given system with heterodimensional cycles is the four-dimensional vector field known as the Atri model [32, 52, 53], but it would be good to find such cycles in a three-dimensional diffeomorphism as well. While the Hénon-like family \mathcal{H} has a blender, its skew product structure prevents it from having heterodimensional cycles. To address this limitation, one could either modify the family \mathcal{H} , explore other versions of extended Hénon maps, for example, the Generalised Hénon map as proposed in [28, 22], or consider a completely different type of diffeomorphisms. Secondly, blenders and also heterodimensional cycles are saddle objects; they may lead to the system exhibiting long chaotic transcients, but are not directly observable from the perspective of real-world models. This is why wild chaotic attractors are an interesting subject of research [7, 23, 27, 26, 37, 40, 48]. A direction we are pursuing, which was already hinted at in [34], is to study the chaotic attractor of \mathcal{H} when $|\xi| \leq 1$ and the parameters α and β are changed so that h has the well-known Hénon attractor.

Acknowledgments

We thank Katsutoshi Shinohara and Andy Hammerlindl for fruitful discussions. The research of BK and HMO has been supported by Royal Society Te Apārangi Marsden Fund grant #22-UOA-204.

Appendix: Relevant curves and ξ -values for switching points and end points

For each of the four cases of orientability discussed in Sections 3.1, 3.2, 4.1 and 4.2, we present here the relevant bounding curves and associated ξ -values of the respective switching points s_j and end points e_j , e_j^- and e_j^+ .

Switching points s_j and end points e_j for $\xi > 1$ and $\beta = -0.3$

| bottom | boundary |
|---------------|------------------------------------------------------------------------------------------------|
| $s_j < \xi$ | ξ -value of s_j |
| $w^{-}(-2)$ | 2.021328 |
| $w^{-}(5)$ | 1.759581 |
| $w^{-}(-8)$ | 1.702157 |
| $w^{-}(17)$ | 1.686919 |
| $w^{-}(-32)$ | 1.681778 |
| $w^{-}(65)$ | 1.680047 |
| $w^{-}(-128)$ | 1.679465 |
| $w^{-}(257)$ | _ |
| $w^{-}(-512)$ | _ |
| | 1.679318 |
| | $s_j < \xi$ $w^-(-2)$ $w^-(5)$ $w^-(-8)$ $w^-(17)$ $w^-(-32)$ $w^-(65)$ $w^-(-128)$ $w^-(257)$ |

| top bo | undary |
|----------------|-----------------------|
| $e_j < \xi$ | ξ -value of e_j |
| $w^{+}(-7)$ | 1.905866 |
| $ w^{+}(-14) $ | 1.847468 |
| $w^{+}(-27)$ | 1.826535 |
| $w^{+}(-54)$ | 1.819414 |
| $w^{+}(-107)$ | 1.816841 |
| $w^+(-214)$ | 1.815907 |
| $w^{+}(-427)$ | 1.815567 |
| $w^{+}(-854)$ | _ |
| $ w^+(-1707) $ | _ |
| | 1.815476 |

Table 7: Switching point and end point data for $\xi > 1$ and $\beta = -0.3$; see Section 3.2.

| | End points e_j^- and e_j^+ for $\xi < -1$ and $\beta = 0.3$ | | | | | | | |
|---------------|-----------------------------------------------------------------|-------------------------|--|-----------------------|-------------------------|--|--|--|
| | | | | | | | | |
| | e_j b | oundary | | e_j b | oundary | | | |
| j | $\xi < e_j^-$ | ξ -value of e_j^- | | $\xi < e_j^+$ | ξ -value of e_j^+ | | | |
| 1 | $w_2^1(11)$ | -1.797432 | | $w_2^2(19)$ | -2.498963 | | | |
| $\mid 2 \mid$ | $ w_2^2(21) $ | -1.740512 | | $oldsymbol{w}_2^1(4)$ | -2.092759 | | | |
| 3 | $ w_2^1(-41) $ | -1.711862 | | $w_2^2(8)$ | -1.926356 | | | |
| $\mid 4 \mid$ | $ w_2^2(-81) $ | -1.696994 | | $w_2^1(-14)$ | -1.857048 | | | |
| 5 | $ w_2^1(163) $ | -1.688870 | | $w_2^2(-28)$ | -1.822392 | | | |
| 6 | $w_2^2(325)$ | -1.684495 | | ${m w}_2^1(56)$ | -1.804822 | | | |
| $ \infty $ | | -1.679392 | | | -1.786754 | | | |

Table 8: End point data for $\xi < -1$ and $\beta = 0.3$; see Section 4.1.

| I | End points e_j^- and e_j^+ for $\xi < -1$ and $\beta = -0.3$ | | | | | | |
|---------------|------------------------------------------------------------------|-------------------------|--|---------------|-------------------------|--|--|
| | e_i^- b | oundary | | e_i^+ b | oundary | | |
| j | $\xi < e_j^-$ | ξ -value of e_j^- | | $\xi < e_j^+$ | ξ -value of e_j^+ | | |
| 1 | $w_2^1(-2)$ | -2.259592 | | $w_2^2(2)$ | -2.759505 | | |
| 2 | $ w_2^2(4) $ | -2.197271 | | $w_2^1(4)$ | -2.319568 | | |
| 3 | $ w_2^1(8) $ | -2.166457 | | $w_2^2(-6)$ | -2.207981 | | |
| $\mid 4 \mid$ | $ w_2^2(-14) $ | -2.166457 | | $w_2^1(-10)$ | -2.149248 | | |
| 5 | $ w_2^1(-26) $ | -2.140228 | | $w_2^2(-20)$ | -2.119152 | | |
| 6 | $w_2^2(52)$ | -2.134830 | | $w_2^1(-40)$ | -2.103595 | | |
| ∞ | | -2.127741 | | | -2.086951 | | |

Table 9: End point data for $\xi < -1$ and $\beta = -0.3$; see Section 4.2.

References

- [1] Flavio Abdenur, Christian Bonatti, Sylvain Crovisier, and Lorenzo J Díaz. Generic diffeomorphisms on compact surfaces. Fundamenta Mathematicae, 187(2):127–159, 2005.
- [2] R. Abraham and S. Smale. Non-genericity of Ω-stability. In *Global Analysis*, volume 14 of *Proceedings* of Symposia in Pure Mathematics, pages 5–8. American Mathematical Society, 1970.
- [3] Pablo Aguirre, Bernd Krauskopf, and Hinke M Osinga. Global invariant manifolds near a Shilnikov homoclinic bifurcation. *Journal of Computational Dynamics*, 1(1):1–38, 2014.
- [4] Kathleen T Alligood, Tim D Sauer, James A Yorke, and JD Crawford. *Chaos: An Introduction to Dynamical Systems*. Springer, 1997.
- [5] Dmitry Victorovich Anosov. Geodesic Flows on Closed Riemann Manifolds with Negative Curvature. American Mathematical Society, 1969.
- [6] J.-C. Ballot and Hugh C. Williams. The Lucas Sequences: Theory and Applications. Springer, 2023.
- [7] R Bamon, J Kiwi, and J Rivera. Wild Lorenz like attractors. arXiv:0508045, 2005.
- [8] C Bonatti, S Crovisier, L. J Daz, and A Wilkinson. What is... a blender?. *Notices of the American Mathematical Society*, 63(10):1175–1178, 2016.
- [9] C Bonatti and L J Díaz. Persistent nonhyperbolic transitive diffeomorphisms. *Annals of Mathematics*, 143(2):357–396, 1996.
- [10] C Bonatti, L J Díaz, and M Viana. Dynamics Beyond Uniform Hyperbolicity. A Global Geometric and Probabilistic Perspective. Springer, New York, 2005.
- [11] Christian Bonatti. Survey towards a global view of dynamical systems, for the C^1 -topology. Ergodic Theory and Dynamical Systems, 31(4):959–993, 2011.
- [12] Christian Bonatti and Lorenzo J Díaz. Robust heterodimensional cycles and generic dynamics. Journal of the Institute of Mathematics of Jussieu, 7(3):469–525, 2008.
- [13] Robert E Bowen, Jean-René Chazottes, and David Ruelle. Equilibrium States and the Ergodic Theory of Anosov Diffeomorphisms. Springer, New York, 2008.
- [14] M.J. Capiński, B Krauskopf, Hinke M Osinga, and P. Zgliczyński. Characterising blenders via covering relations and cone conditions. arXiv preprint 2212.04861, 2023.
- [15] D C'Julio, B Krauskopf, and Hinke M Osinga. Computing parametrised large intersection sets of 1D invariant manifolds: a tool for blender detection. *Numerical Algorithms*, 96:1079–1108, 2024.
- [16] L J Díaz, S Kiriki, and K Shinohara. Blenders in centre unstable Hénon-like families: With an application to heterodimensional bifurcations. *Nonlinearity*, 27(3):353–378, 2014.
- [17] Lorenzo J Díaz. Robust nonhyperbolic dynamics and heterodimensional cycles. *Ergodic Theory and Dynamical Systems*, 15(2):291–315, 1995.
- [18] Eusebius J Doedel, Bernd Krauskopf, and Hinke M Osinga. Global invariant manifolds in the transition to preturbulence in the Lorenz system. *Indagationes Mathematicae*, 22(3-4):222–240, 2011.
- [19] Zbigniew Galias. Positive topological entropy of Chua's circuit: A computer assisted proof. *International Journal of Bifurcation and Chaos*, 7(02):331–349, 1997.
- [20] NK Gavrilov and LP Shilnikov. On three-dimensional dynamical systems close to systems with a structurally unstable homoclinic curve. I. *Mathematics of the USSR-Sbornik*, 17(4):467, 1972.
- [21] Sergei Vladimirovich Gonchenko, James D Meiss, and Ivan Ilich Ovsyannikov. Chaotic dynamics of three-dimensional Hénon maps that originate from a homoclinic bifurcation. *Regular and Chaotic Dynamics*, 11(2):191–212, 2006.
- [22] Sergey Gonchenko, Ming-Chia Li, and Mikhail Malkin. Generalized Hénon maps and Smale horse-shoes of new types. *International Journal of Bifurcation and Chaos*, 18(10):3029–3052, 2008.

- [23] Sergey V Gonchenko, II Ovsyannikov, C Simó, and Dmitry Turaev. Three-dimensional Hénon-like maps and wild Lorenz-like attractors. *International Journal of Bifurcation and Chaos*, 15(11):3493–3508, 2005.
- [24] Sergey V Gonchenko, Leonid P Shilnikov, and Dmitry V Turaev. Dynamical phenomena in systems with structurally unstable Poincaré homoclinic orbits. Chaos: An Interdisciplinary Journal of Nonlinear Science, 6(1):15–31, 1996.
- [25] S.V. Gonchenko, A.S. Gonchenko, and M.I. Malkin. On Local Topological Classification of Two-Dimensional Orientable, Non-Orientable, and Half-Orientable Horseshoes. Springer, New York, 2018.
- [26] S.V. Gonchenko, A.O. Kazakov, and D.V. Turaev. Wild pseudohyperbolic attractors in a four-dimensional Lorenz system. *Nonlinearity*, 34(4):2018–2047, 2021.
- [27] S.V. Gonchenko, L.P. Shilnikov, and D.V. Turaev. On global bifurcations in three-dimensional diffeomorphisms leading to wild Lorenz-like attractors. *Regular and Chaotic Dynamics*, 14(1):137–147, 2009.
- [28] V. S Gonchenko, Y. A Kuznetsov, and H. G. E. Meijer. Generalized Hénon map and bifurcations of homoclinic tangencies. SIAM Journal on Applied Dynamical Systems, 2(4):407–436, 2005.
- [29] Celso Grebogi, Edward Ott, and James A Yorke. Crises, sudden changes in chaotic attractors, and transient chaos. *Physica D: Nonlinear Phenomena*, 7(1-3):181–200, 1983.
- [30] Celso Grebogi, Edward Ott, and James A Yorke. Basin boundary metamorphoses: changes in accessible boundary orbits. *Nuclear Physics B Proceedings Supplements*, 2:281–300, 1987.
- [31] John Guckenheimer and Philip Holmes. Nonlinear Oscillations, Dynamical Systems, and Bifurcations of Vector Fields. Springer, New York, 2013.
- [32] Andy Hammerlindl, Bernd Krauskopf, Gemma Mason, and Hinke M Osinga. Determining the global manifold structure of a continuous-time heterodimensional cycle. *Journal of Computational Dynamics*, 9:393–419, 2022.
- [33] Michel Hénon. A two-dimensional mapping with a strange attractor. Communications in Mathematical Physics, 50:69–77, 1976.
- [34] S Hittmeyer, B Krauskopf, H M Osinga, and K Shinohara. Existence of blenders in a Hénon-like family: Geometric insights from invariant manifold computations. *Nonlinearity*, 31(10):R239–R267, 2018
- [35] S Hittmeyer, B Krauskopf, H M Osinga, and K Shinohara. How to identify a hyperbolic set as a blender. Discrete & Continuous Dynamical Systems, 40(12):6815–6836, 2020.
- [36] S Hittmeyer, B Krauskopf, H M Osinga, and K Shinohara. Boxing-in of a blender in a Hénon-like family. Frontiers in Applied Mathematics and Statistics, 9:1086240, 2023.
- [37] S. Hittmeyer, B. Krauskopf, and H.M Osinga. From wild Lorenz-like to wild Rovella-like dynamics. *Dynamical Systems*, 30(4):525–542, 2015.
- [38] Stefanie Hittmeyer, Bernd Krauskopf, and Hinke M Osinga. Interacting global invariant sets in a planar map model of wild chaos. SIAM Journal on Applied Dynamical Systems, 12(3):1280–1329, 2013
- [39] A. F. Horadam. Jacobsthal representation numbers. The Fibonacci Quarterly, 34(1):40-54, 1996.
- [40] H. Jelleyman and H.M. Osinga. Matching geometric and expansion characteristics of wild chaotic attractors. *The European Physical Journal Special Topics*, 231(3):403–412, 2022.
- [41] Yuri A. Kuznetsov. Elements of Applied Bifurcation Theory. Springer, 1998.
- [42] H. G. E. Meijer, W. Govaerts, Yuri A. Kuznetsov, R. Khoshsiar Ghaziani, and N. Neirynck. Mat-ContM: A toolbox for continuation and bifurcation of cycles of maps: Command line use. *Universiteit Gent, Belgium, and Utrecht University, The Netherlands*, 2017.

- [43] Christian Mira. Chaotic Dynamics: From the One-Dimensional Endomorphism to the Two-Dimensional Diffeomorphism. World Scientific, 1987.
- [44] C G Moreira. There are no C^1 stable intersections of regular Cantor sets. Acta Mathematica, 206:311–323, 2011.
- [45] S. E Newhouse. The abundance of wild hyperbolic sets and nonsmooth stable sets for diffeomorphisms. *Publications Mathématiques IHÉS*, 50:101–151, 1979.
- [46] Edward Ott. Chaos in Dynamical Systems. Cambridge University Press, 2002.
- [47] J Jr Palis and Welington De Melo. Geometric Theory of Dynamical Systems: An Introduction. Springer, New York, 2012.
- [48] Y Saiki, M.A.F. Sanjuán, and J.A. Yorke. The continuous route to multi-chaos. *Preprint*, page arxiv:1802.04777, 2018.
- [49] Stephen Smale. Differentiable dynamical systems. Bulletin of the American Mathematical Society, 73(6):747–817, 1967.
- [50] Steven H Strogatz. Nonlinear Dynamics and Chaos: With Applications to Physics, Biology, Chemistry, and Engineering. CRC Press, 2018.
- [51] Laura Tedeschini-Lalli and James A Yorke. How often do simple dynamical processes have infinitely many coexisting sinks? *Communications in Mathematical Physics*, 106(4):635–657, 1986.
- [52] Nelson Wong, Bernd Krauskopf, and Hinke M. Osinga. Cascades of heterodimensional cycles via period doublings. Communications in Nonlinear Science and Numerical Simulation, 140(1):108328, 2025.
- [53] Wenjun Zhang, Bernd Krauskopf, and Vivien Kirk. How to find a codimension-one heteroclinic cycle between two periodic orbits. *Discrete and Continuous Dynamical Systems A*, 32(8):2825–2851, 2012.